

Simulations of Severe Convective Systems Using 1- versus 3-km Grid Spacing

MORRIS L. WEISMAN,^a KEVIN W. MANNING,^a RYAN A. SOBASH,^a AND CRAIG S. SCHWARTZ^a

^a National Center for Atmospheric Research, Boulder, Colorado

(Manuscript received 17 June 2022, in final form 17 October 2022)

ABSTRACT: Herein, 14 severe quasi-linear convective systems (QLCS) covering a wide range of geographical locations and environmental conditions are simulated for both 1- and 3-km horizontal grid resolutions, to further clarify their comparative capabilities in representing convective system features associated with severe weather production. Emphasis is placed on validating the simulated reflectivity structures, cold pool strength, mesoscale vortex characteristics, and surface wind strength. As to the overall reflectivity characteristics, the basic leading-line trailing stratiform structure was often better defined at 1 versus 3 km, but both resolutions were capable of producing bow echo and line echo wave pattern type features. Cold pool characteristics for both the 1- and 3-km simulations were also well replicated for the differing environments, with the 1-km cold pools slightly colder and often a bit larger. Both resolutions captured the larger mesoscale vortices, such as line-end or bookend vortices, but smaller, leading-line mesoscale updraft vortices, that often promote QLCS tornadogenesis, were largely absent in the 3-km simulations. Finally, while maximum surface winds were only marginally well predicted for both resolutions, the simulations were able to reasonably differentiate the relative contributions of the cold pool versus mesoscale vortices. The present results suggest that while many QLCS characteristics can be reasonably represented at a grid scale of 3 km, some of the more detailed structures, such as overall reflectivity characteristics and the smaller leading-line mesoscale vortices would likely benefit from the finer 1-km grid spacing.

SIGNIFICANCE STATEMENT: High-resolution model forecasts using 3-km grid spacing have proven to offer significant forecast guidance enhancements for severe convective weather. However, it is unclear whether additional enhancements can be obtained by decreasing grid spacings further to 1 km. Herein, we compare forecasts of severe quasi-linear convective systems (QLCS) simulated using 1- versus 3-km grids to document the potential value added of such increases in grid resolutions. It is shown that some significant improvements can be obtained in the representation of many QLCS features, especially as regards reflectivity structure and in the development of small, leading-line mesoscale vortices that can contribute to both severe surface wind and tornado production.


KEYWORDS: Mesoscale forecasting; Numerical weather prediction/forecasting; Short-range prediction; Cloud resolving models

1. Introduction

Quasi-linear convective systems (QLCSs) represent one of the more common modes of convective organization and are responsible for a significant percentage of severe convective weather events, including high winds, hail, flooding, and tornadoes (e.g., Ashley et al. 2019; Smith et al. 2012; Thompson et al. 2012; Trapp et al. 2005). Often, such severe weather exhibits bow echoes or line-echo wave pattern (LEWP) radar reflectivity configurations, which in turn are associated with strong surface cold pools and straight-line surface winds (e.g., Przybylinski 1995). Mesoscale circulations such as along-line vortices (e.g., Wakimoto et al. 2006; Atkins and St. Laurent 2009; Wheatley and Trapp 2008; Weisman and Trapp 2003; Trapp and Weisman 2003) and line-end (or bookend) vortices (e.g., Weisman and Davis 1998) are also common features of such systems and can contribute to the production of severe surface winds and tornadoes (e.g., Przybylinski and Schmocker 1993; Pfost and Gerard 1997; Atkins et al. 2004).

Convection allowing models (CAMs) with horizontal grid spacing of ~4 km or less have become highly valued tools for predicting hazardous convective weather (e.g., Kain et al. 2008; Weisman et al. 2008). The ability to forecast differing convective modes, such as supercells versus QLCSs, which help guide the characterization of the severe weather threat, has been an important component of this success. In this regard, both idealized and case study simulations using 3–4-km grid resolutions have generally been found to be sufficient to reasonably represent the mesoscale aspects of QLCSs, including bowing convective lines, rear inflow jets, and mesoscale vortices (e.g., Weisman 1993; Weisman and Davis 1998; Cram et al. 2002; Weisman et al. 2013; Xu et al. 2015).

Still, some deficiencies have also been documented when using 3–4-km grid spacing, presumably due to an inability to properly represent the physical processes critical for some of the convective hazards. Hepper et al. (2016) described two cases where convective winds were underforecast in their 4-km Δx forecasts, suggesting the deficiency was due to the inability to resolve processes related to the production of near-surface convective gusts. In their tornado forecasts, Gallo et al. (2016,

 Denotes content that is immediately available upon publication as open access.

Corresponding author: Morris L. Weisman, weisman@ucar.edu

Publisher's Note: This article was revised on 2 March 2023 to correct a typographical error in the last entry in Table 1.

DOI: 10.1175/WAF-D-22-0112.1

© 2023 American Meteorological Society. For information regarding reuse of this content and general copyright information, consult the [AMS Copyright Policy](#) (www.ametsoc.org/PUBSReuseLicenses).

TABLE 1. The 14 MCS cases used in the present study, including estimated representative environmental CAPE (J kg^{-1}), 0–6-km vertical wind shear (kt), cold pool strength θ'_v (K), cold pool pressure change ΔP (hPa), and maximum wind gusts (kt) (ASOS/storm reports), as determined from ASOS surface observations and severe storm reports, as described in the text.

Cases	Location	CAPE (J kg^{-1})	0–6-km shear (kt)	θ'_v (K)	ΔP (hPa)	Max wind (kt)
27 Apr 2011	AL	1250	30	8.5	7	72/90
29 Jun 2012	OH	5500	20	16	8	80/91
19 May 2013	KS	4500	25	10	6	60/80
12 Jun 2013	IL, IN	4500	30	9	5	87/95
28 Apr 2014	MS, AL	4500	30	7	5	50/70
30 Jun 2014	IA, IL	5000	30	10	7	70/90
22 Jun 2015	IA, IL	2200	30	10	7	70/93
13 Jul 2015	IN, KY	5000	15	8	4	58/70
23 Dec 2015	AR, TN, KY	1250	40	7	4	49/90
31 Mar 2016	MS, AL	2500	30	4	3	35/80
26 Apr 2016	TX, OK, KS	4500	25	11	7	54/91
30 Nov 2016	GA	750	40	7	3	41/60
28 Feb 2017	MS, AR, KY	2000	40	9	5	64/80
10 Aug 2020	IA, IL, IN	5500	15	16	7	107/110

2018, 2019) similarly suggested that 3–4-km Δx CAMs were unable to represent processes leading to intense low-level rotation. Errant storm motions have also been noted in 3–4-km Δx forecasts of both supercells (VandenBerg et al. 2014) and

MCSs (Schwartz et al. 2017). Similar deficiencies have been identified in idealized studies using simplified cloud models, for processes such as mesocyclone cycling (Adlerman and Droegemeier 2002), low-level vorticity intensification

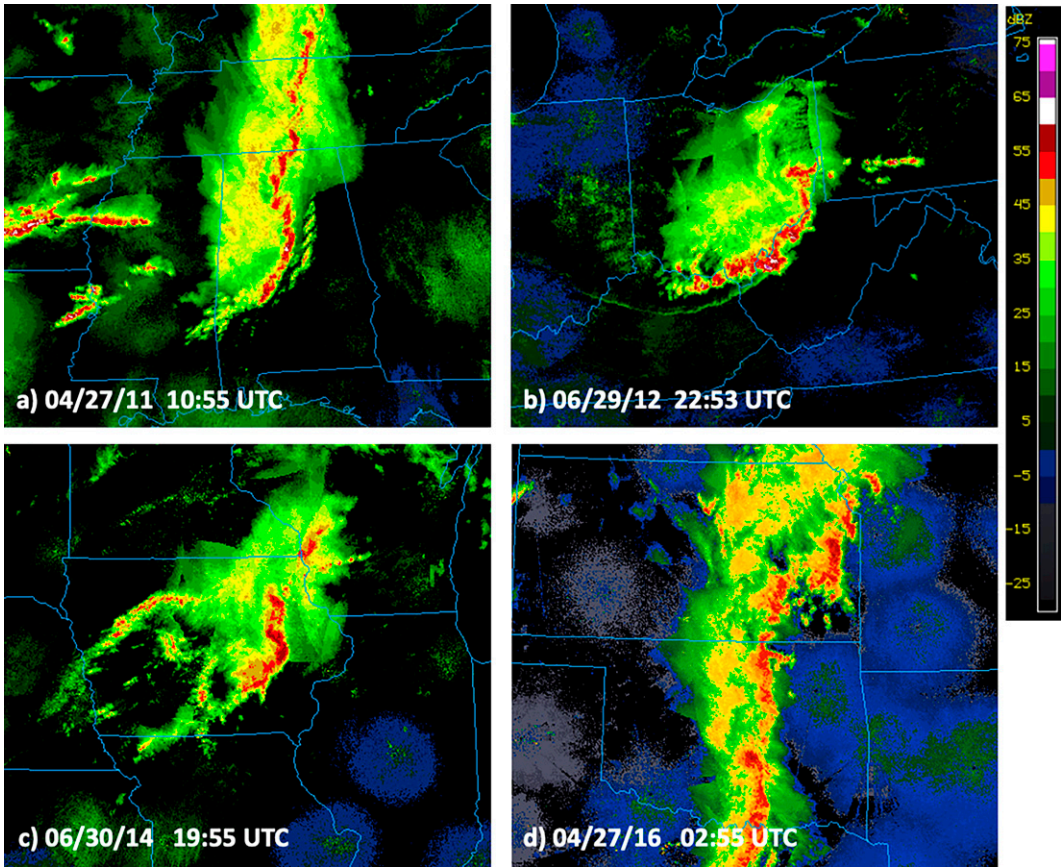


FIG. 1. Observed representative composite reflectivity (dBZ) for four sample cases included in this study for (a) 1055 UTC 27 Apr 2011, (b) 2253 UTC 29 Jun 2012, (c) 1955 UTC 30 Jun 2014, and (d) 0255 UTC 27 Apr 2016.

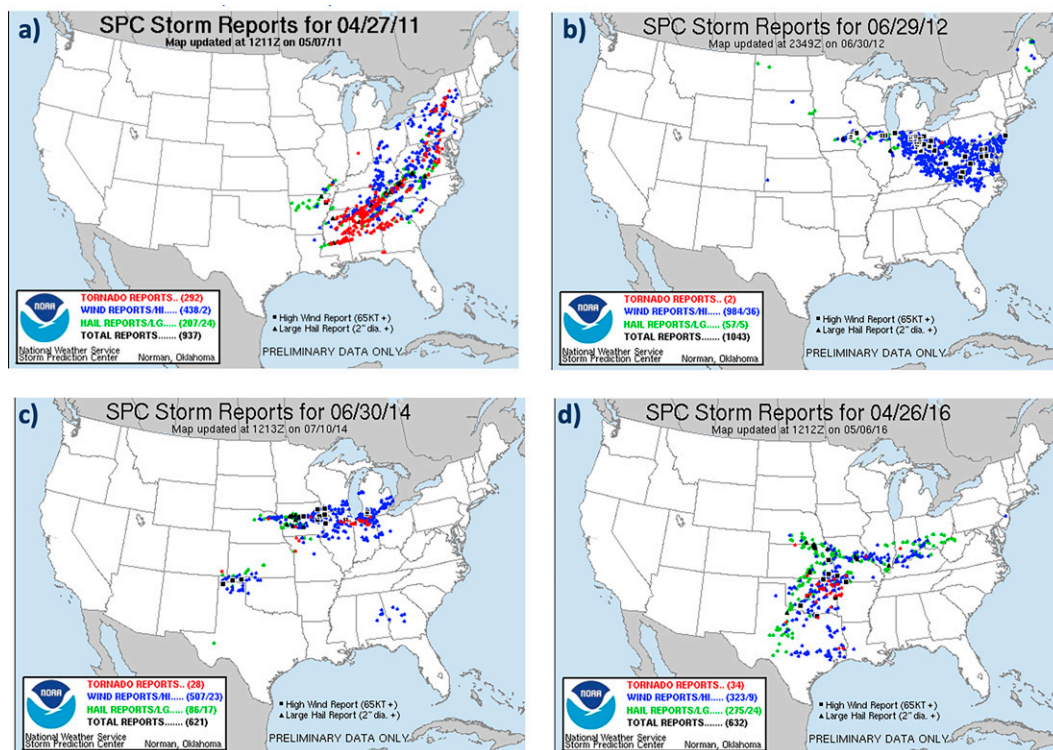


FIG. 2. SPC storm reports for (a) 27 Apr 2011, (b) 29 Jun 2012, (c) 30 Jun 2014, and (d) 26 Apr 2016.

(Potvin and Flora 2015), and updraft and downdraft strength (e.g., Bryan et al. 2003; Bryan and Morrison 2012).

Increasing grid resolution to 1 km improves the representation of some Q LCS features, such as more detailed and realistic reflectivity structures and more realistic updraft and downdraft strengths (e.g., Kain et al. 2008; Schwartz et al. 2017; Bryan et al. 2003; Bryan and Morrison 2012) as well as the tendency to develop smaller scale mesoscale vortices that often develop along the leading edge and ends of such systems (e.g., Weisman and Trapp 2003; Trapp and Weisman 2003; Atkins and St. Laurent 2009; Atkins et al. 2004; Wheatley and Trapp 2008; Xu et al. 2015). However, when considering overall precipitation and severe weather production, some studies of next-day CAM forecasts have documented minimal benefit to moving toward 1-km Δx (e.g., Kain et al. 2008; Schwartz et al. 2009; Clark et al. 2012; Johnson et al. 2013; Loken et al. 2017).

More recently, Schwartz et al. (2017) considered the relative value of using 1- versus 3-km ensembles for forecasting severe convection during the 15 May–15 June 2013 MPEX field campaign (e.g., Weisman et al. 2015). They found that 10-member 1-km probabilistic forecasts produced better precipitation forecasts than 3-km probabilistic forecasts over the first 12 h and for heavier rain rates. Additionally, 1-km cold pool deficits were slightly larger than 3-km deficits, and 1-km MCS centroids were regularly farther southeast than 3-km objects, suggesting that 1-km MCSs moved faster to the east and south than 3-km MCSs. Overall, the 1-km MCS locations agreed better with the observed systems. Schwartz and Sobash (2019) and Sobash et al. (2019) further considered the impact of

increasing grid resolutions from 3 to 1 km for 497 cases of severe thunderstorms east of the Rocky Mountains between 2010 and 2017, noting improvements in both next day precipitation characteristics (e.g., timing and location of the convection) and next day tornado guidance, especially for relatively large convective systems. However, they also noted that the more positive results using 1-km Δx as compared to earlier studies might be related to improvements in the initial conditions in these later studies.

Additionally, Thielen and Gallus (2019) simulated 10 nocturnal convective systems in weakly forced environments at 3 and 1 km using WRF-ARW with four different microphysics schemes. The WRF-ARW underpredicted linear modes and overpredicted cellular modes at 3 km for all of the microphysics schemes. The proportion of linear systems increased using 1-km Δx , but this improvement was insufficient to match observations or show more forecast accuracy. Similarly, Squitieri and Gallus (2020) used WRF-ARW to simulate 14 leading line/trailing stratiform MCSs from the Great Plains and Upper Mississippi Valley with 3-, 1-, and 0.33-km grids to study the sensitivity of cold pool behavior and MCS propagation to grid spacing. Cold pools were larger using finer grids. The 1-km grids slightly increased both the 3-h QPF forecast skill and 9-h precipitation swath alignment compared to 3 km, but the 3-km MCS speed was closer to observed than for the 1-km MCS. The observed cold pool strengths, however, were not documented.

In the present paper, we present a companion study to Schwartz and Sobash (2019) and Sobash et al. (2019), as well as extending the work of Thielen and Gallus (2019) and

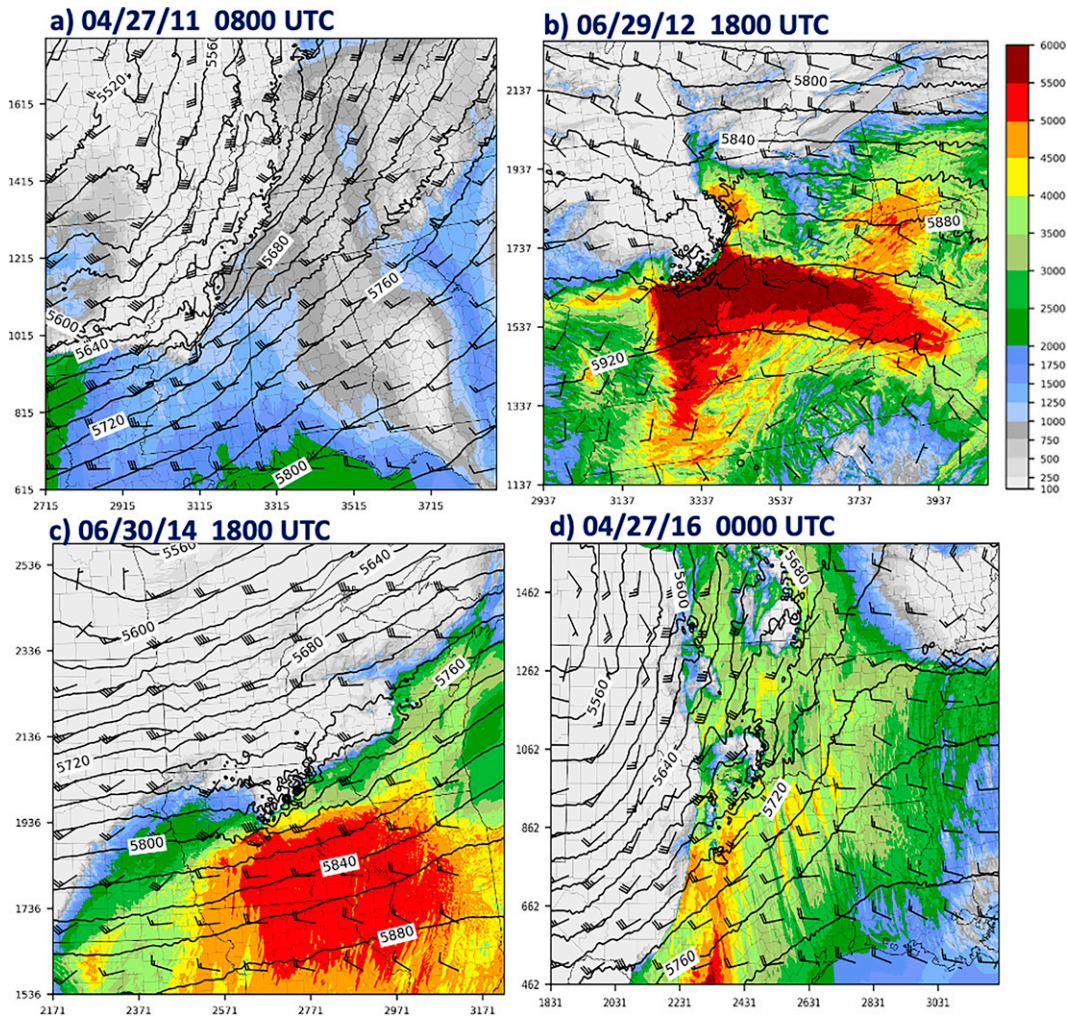


FIG. 3. 500-hPa heights (contoured), most unstable CAPE (MUCAPE; J kg^{-1} ; shaded), and 0–6-km vertical wind shear (kt; wind barbs) at representative times for the (a) 27 Apr 2011, (b) 29 Jun 2012, (c) 30 Jun 2014, and (d) 26 Apr 2016 events, as diagnosed from the 1-km WRF-ARW simulations. Wind shear barbs are spaced 100 km apart.

Squitieri and Gallus (2020), to further investigate the impacts of resolution on QLCS structure, with specific focus on characteristics often associated with severe weather production. For this purpose, 14 severe QLCS cases, considering a wide range of convective system structures and environmental conditions, were chosen from the Schwartz and Sobash (2019) and Sobash et al. (2019) studies for more in-depth analysis. The 1- and 3-km simulations are compared to the observed systems, with emphasis placed on documenting reflectivity features, cold pool and mesovortex characteristics, and the resulting surface wind structure and strength, as related to severe weather production, which was not addressed in the previous studies. Given the importance of cold pools to overall QLCS structure and evolution, we also attempt to validate the simulated cold pool characteristics relative to the observed cold pools, which was also not included in these previous studies.

We begin in section 2 with a description of the methodology used in the present study, followed in section 3 by an

overview of four of the more notable cases, emphasizing the range of environments and structural features considered in the present study. Sections 4–6 then present a more detailed analysis of the observed and simulated cold pools, mesoscale vortices, and surface wind characteristics, followed in section 7 by a summary and comparison to the previous studies noted above.

2. Methods

a. Case selection

The set of 14 severe QLCSs that were chosen from the Schwartz and Sobash (2019) and Sobash et al. (2019) studies are listed in Table 1 along with some of their basic environmental characteristics. These cases represent a wide range of synoptic environments, seasons, and geographical locations, and all produced significant severe weather outbreaks. Some

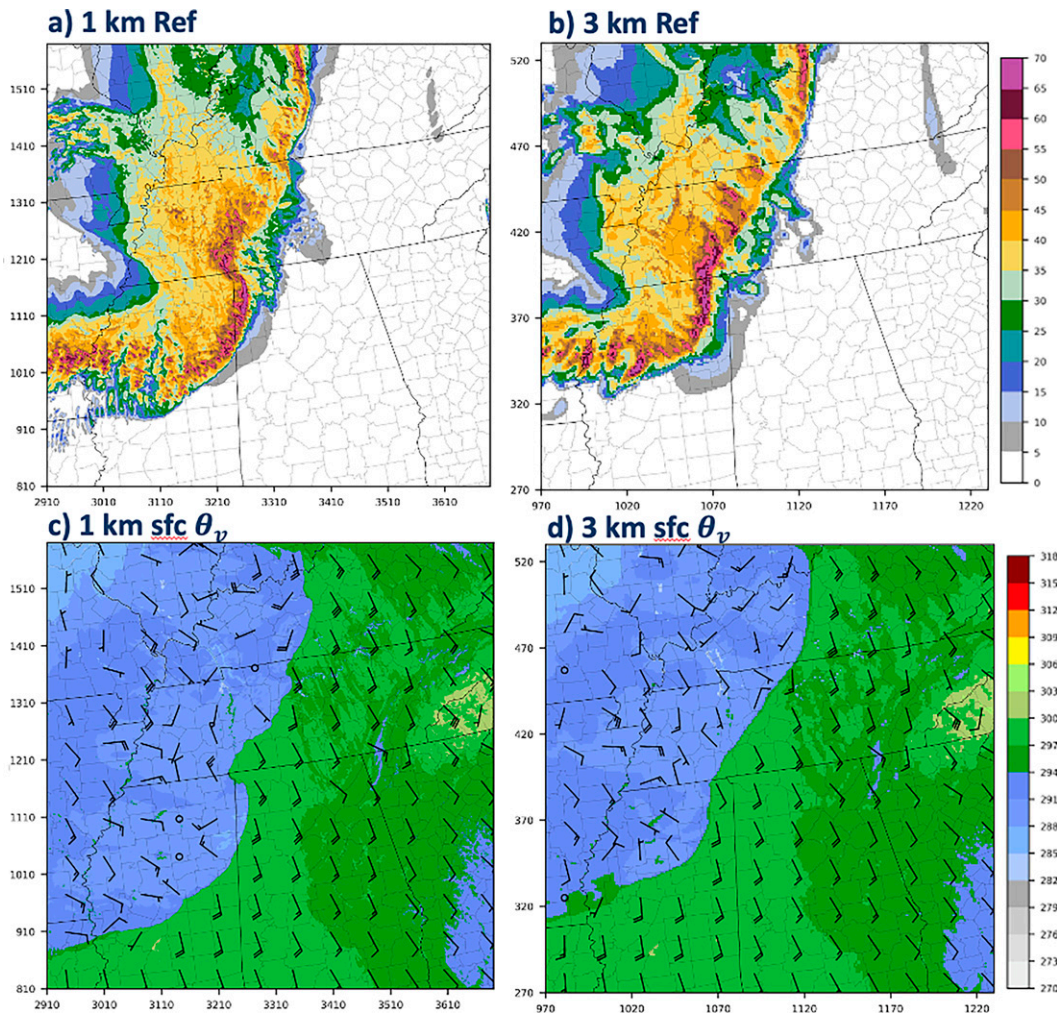


FIG. 4. (a),(b) Composite reflectivity (Ref; dBZ) and (c),(d) surface winds (kt) and surface θ_v (K) from the 1- vs 3-km WRF-ARW simulations, respectively, for 1000 UTC 27 Apr 2011 (10-h forecast). Wind barbs are spaced 66 km apart.

of the more noteworthy events include the 27 April 2011 tornado outbreak in the southeastern United States, for which there was a severe QLCS producing several tornadoes and damaging straight line winds early in the morning prior to the main afternoon event (e.g., Knupp et al. 2014), the 29 June 2012 derecho that produced a swath of severe wind damage from Indiana to Washington, D.C., the 26 April 2016 severe weather outbreak in Texas, Oklahoma, and Kansas, for which a highly anticipated supercell tornado outbreak evolved instead into an extensive squall line with more localized tornado and severe wind events, and the 30 June 2014 severe bow echo that passed through Iowa and southern Wisconsin, producing winds over 90 mph along with extensive tree damage and power outages. These four cases are described in more detail to highlight the range of characteristic structural features often associated with such convective systems.

b. Model configuration

The 3- and 1-km Δx were produced using version 3.6.1 of the Advanced Research version of the Weather Research and

Forecasting (WRF) Model (Skamarock et al. 2008; Powers et al. 2017) as described in Sobash et al. (2019). Both sets of forecasts were initialized at 0000 UTC by interpolating 0000 UTC 0.5° Global Forecast System (GFS) analyses onto the 3- and 1-km domains and used 3-hourly 0.5° GFS forecasts as lateral boundary conditions. The subsequent convective systems of interest developed roughly 9–24 h after initialization, which is generally considered sufficient to avoid model spinup issues. All forecasts used a computational domain spanning the entire CONUS, with 40 vertical levels and a 50-hPa model top, and were run for 36 h. Physical parameterizations included Thompson microphysics (Thompson et al. 2008), the Mellor–Yamada–Janjić (MYJ) planetary boundary layer (Mellor and Yamada 1982; Janjić 1994, 2002), the Noah land surface model (Chen and Dudhia 2001), and the Rapid Radiative Transfer Model for Global Climate Models (RRTMG) for longwave and shortwave radiation (Mlawer et al. 1997; Iacono et al. 2008; Tegen et al. 1997). The time step was set to 4 times Δx for both sets of forecasts (i.e., 4 s for the 1-km Δx forecasts and 12 s for the 3-km Δx forecasts).

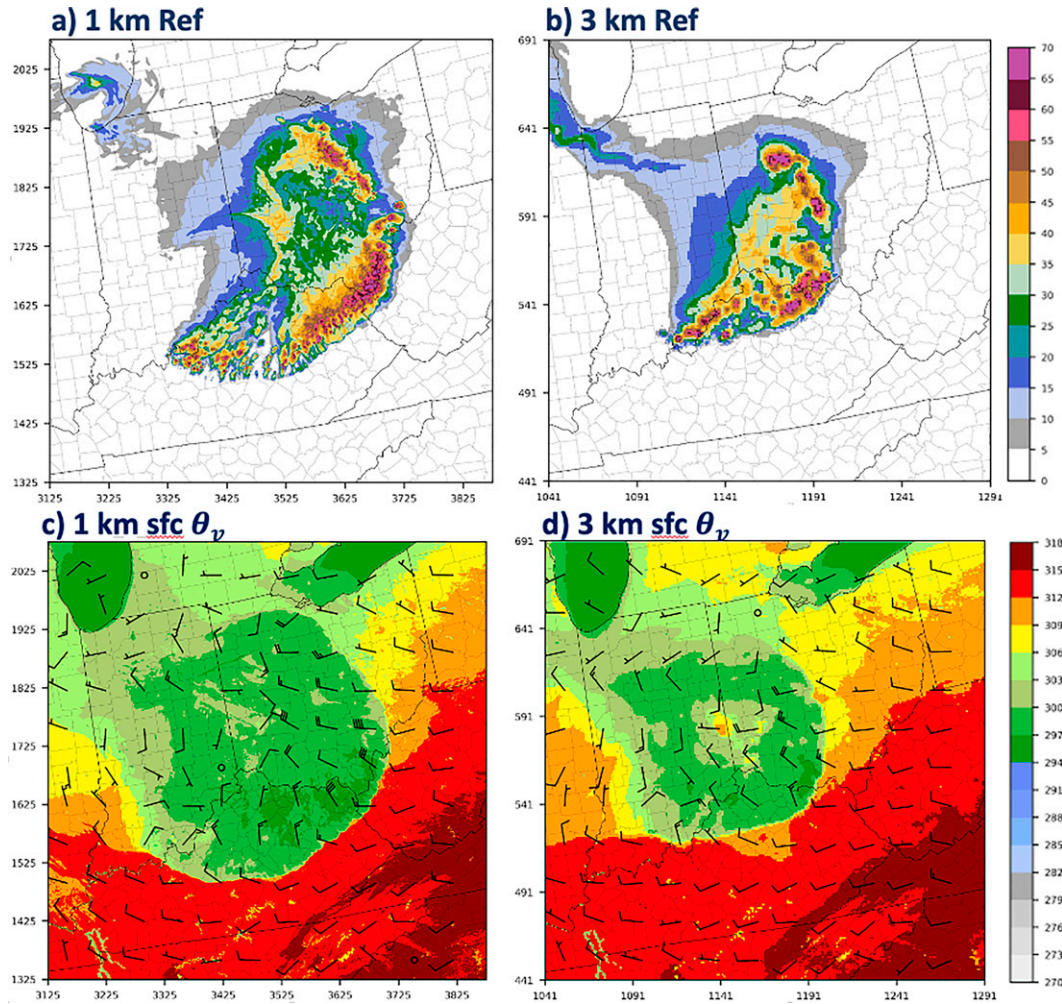


FIG. 5. (a),(b) Composite reflectivity (Ref; dBZ) and (c),(d) surface winds (kt) and surface θ_v (K) from the 1- vs 3-km WRF-ARW simulations, respectively, for 2100 UTC 29 Jun 2012 (21-h forecast). Wind barbs are spaced 66 km apart.

c. Cold pool characteristics

The strength, structure, and propagation characteristics of convective systems are strongly dependent on the system-generated cold pool (e.g., Rotunno et al. 1988; Weisman and Rotunno 2004). Cold pool strength is often estimated by calculating the theoretical propagation speed C of an equivalent density current in a pristine environment (e.g., ignoring contributions from precipitation loading and any convective circulation extending above the cold pool; e.g., Trier et al. 2006), given by

$$C^2 = 2 \int_0^H -g \left(\frac{\theta'_v}{\theta_v} \right) dz,$$

where θ_v represents the environmental virtual potential temperature, θ'_v represents the virtual potential temperature difference across the cold pool interface, and H represents the cold pool depth (e.g., Benjamin 1968). However, H is generally not easily observed, making it difficult to estimate C using this formulation. Alternately, C can be expressed in terms of

the pressure change across the cold pool interface ΔP assuming hydrostatic conditions and no convection above:

$$C = \sqrt{2 \frac{\Delta P}{\bar{\rho}}},$$

where $\bar{\rho}$ represents the mean density. An advantage of using this formulation is that it inherently accounts for cold pool depth, since for a pure density current, the ΔP would represent the vertical integral of θ'_v within the cold pool. However, a disadvantage is that the pressure field is often highly perturbed in the vicinity of such cold pools due to convectively produced gravity waves, making it difficult to distinguish the ΔP simply associated with the cold pool alone. Even given these caveats, both θ'_v and ΔP are found to be useful surrogates for cold pool strength for comparison among the different cases, as we will also employ herein.

Cold pool characteristics were further documented using the equivalent potential temperature θ_e , which is generally

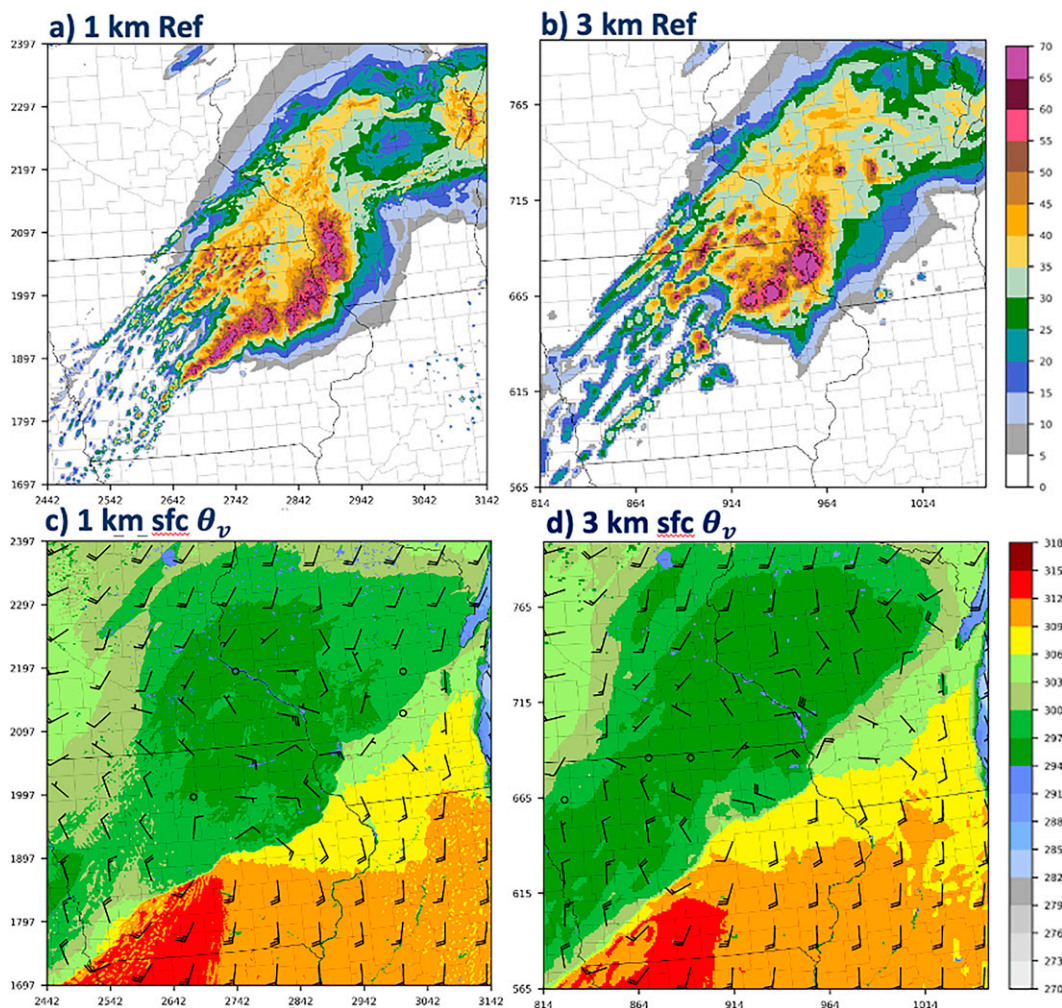


FIG. 6. (a),(b) Composite reflectivity (Ref; dBZ) and (c),(d) surface winds (kt) and surface θ_v (K) from the 1- vs 3-km WRF-ARW simulations, respectively, for 2000 UTC 30 Jun 2014 (20-h forecast). Wind barbs are spaced 66 km apart.

conserved in these convective systems and can be used to identify the source region for the system-scale downdrafts (e.g., the potentially coldest surface outflow in such systems often originates from the midtroposphere, from the level of minimum environmental θ_e). Thus, differences between the observed and simulated cold pool θ_e could indicate significant differences in the cold pool source regions.

The θ'_v , ΔP , and θ_e associated with the cold pools were documented for both the observed and simulated convective systems using 5-min time series from available Automated Surface Observation System (ASOS) data and saved model output at 10 m AGL. A time of cold pool passage was objectively identified at each location or model grid point by a drop of at least 6 K in θ_e , which would represent a clear change in airmass characteristics. Cold pool characteristics were then diagnosed by calculating the differences for each parameter using averaged magnitudes for 30 min before the start and after the end of the identified drop in θ_e , to represent environmental conditions and cold pool conditions, respectively. For both the observations and simulations, the “maximum” thermodynamic characteristics were defined as

the maximum change in magnitude of the variable in the interval 30 min before and after the cold pool’s passage.

d. Mesoscale vortex characteristics

The common association of embedded and line-end mesoscale vortices with severe weather within convective systems motivates the need to document the capabilities of using 1- versus 3-km Δx to simulate such features. Such mesoscale vortices occur over a fairly large range of scales, from just a few kilometers for many of the leading-line vortices responsible for producing QLCS tornadoes, to tens of kilometers for some line-end vortices that can produce similarly large swaths of damaging straight-line winds. Thus, it is important to document the ability of these simulations to reproduce this full range of observed mesoscale vortex scales.

Mesoscale vortices can often be identified operationally using Doppler winds when the radar is favorably positioned relative to the convective system (e.g., relatively close, and directly

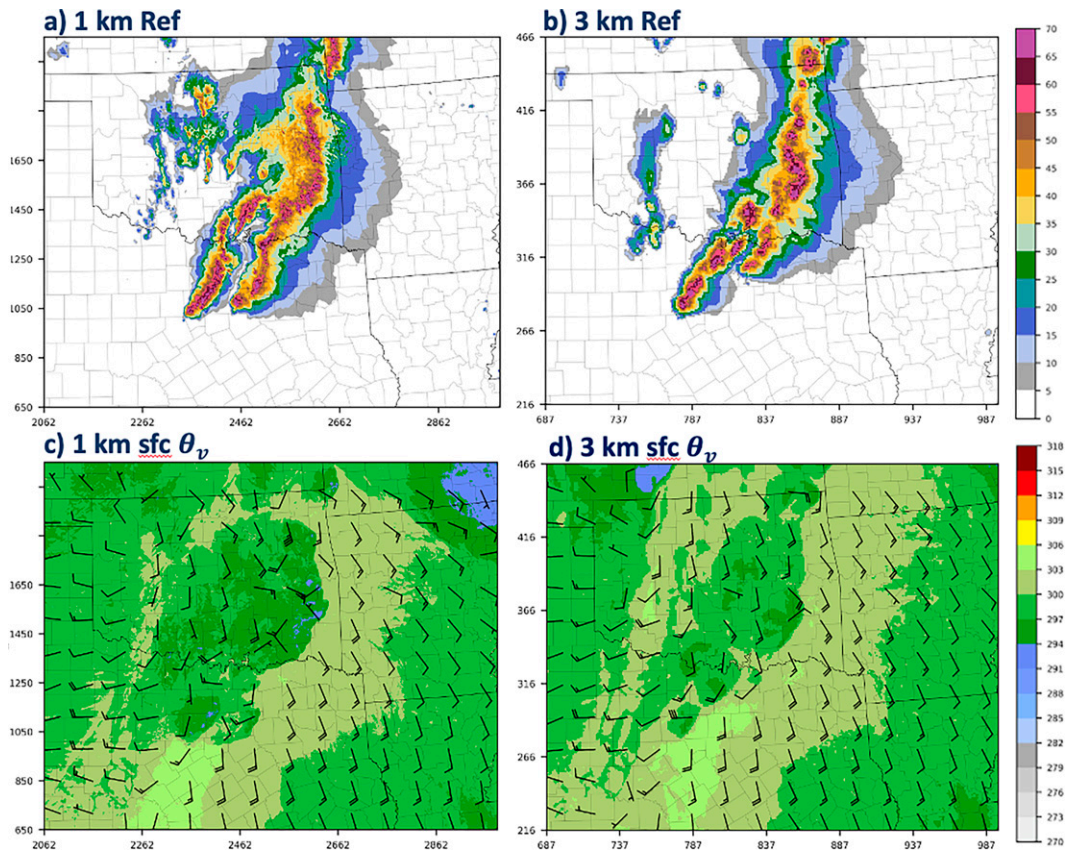


FIG. 7. (a),(b) Composite reflectivity (Ref; dBZ) and (c),(d) surface winds (kt) and surface θ_v (K) from the 1- vs 3-km WRF-ARW simulation, respectively, for 0300 UTC 27 Apr 2016 (27-h forecast). Wind barbs are spaced 66 km apart.

downstream or upstream of the convective system relative to system motion). They are also often associated with bow echo or embedded LEWP reflectivity features, which can be identified using radar reflectivity at larger distances and any angle. Thus, both winds and model-generated reflectivity are used to identify comparable features in the simulations.

Many convective mesoscale vortices, especially those that produce QLCS tornadoes, are associated with strong updrafts, which can be readily identified in the simulations using updraft helicity (UH; Kain et al. 2008). The physical model on which UH is based is that of a supercell storm, composed of a midlevel rotating updraft along with a low-level rotating updraft that at times can be tornadic. As such, 2–5 km above ground level (AGL) UH is found to be very helpful in identifying midlevel supercell structures in 1–3-km CAM forecasts, with 0–1-km UH then adding further guidance as to the probability that the supercell may be tornadic (e.g., Kain et al. 2008, 2010; Sobash et al. 2011; Naylor et al. 2012). Extreme values of UH have also been used to produce next-day guidance for the combined threat from all severe hazards [i.e., hail ≥ 1 in., wind gusts ≥ 50 kt ($1 \text{ kt} \approx 0.51 \text{ m s}^{-1}$), and/or tornadoes, e.g., Sobash et al. 2011, 2016]. Although not all mesoscale vortices within QLCSs are necessarily associated with

updrafts and subsequently high values of UH, the apparent association of high UH with many of the severe weather phenomena in such systems (e.g., especially QLCS tornadoes) makes it a useful parameter to help characterize the severe weather potential of such systems.

Herein, we use 0–1 km AGL updraft helicity (UH01) to help identify such potentially significant low-level mesoscale vortices. In WRF, this is computed as a summation of updraft speed times vertical vorticity, multiplied by the layer depth, using model levels between 0 and 1 km AGL. Diagnostics were computed each time step during the WRF integration and stored as hourly maximum values, as in Kain et al. (2010). It should be noted that the magnitudes of UH01 are scale dependent: e.g., based on simple linear scaling of vertical velocity and vertical vorticity one would expect a factor of about 9 times increase in UH01 magnitudes for 1- versus 3-km gridscale resolutions. Consistent with this approximate scaling, Sobash et al. (2019) found critical minimum values of UH01 for severe weather prediction of $4.7 \text{ m}^2 \text{ s}^{-2}$ for 3-km simulations, increasing to $34.6 \text{ m}^2 \text{ s}^{-2}$ for the equivalent 1-km simulations. For the current set of simulations, it was found useful to use a 0–10 $\text{m}^2 \text{ s}^{-2}$ scale for UH01 for the 3-km simulations and a 0–80 $\text{m}^2 \text{ s}^{-2}$ scale for UH01 for the 1-km simulations.

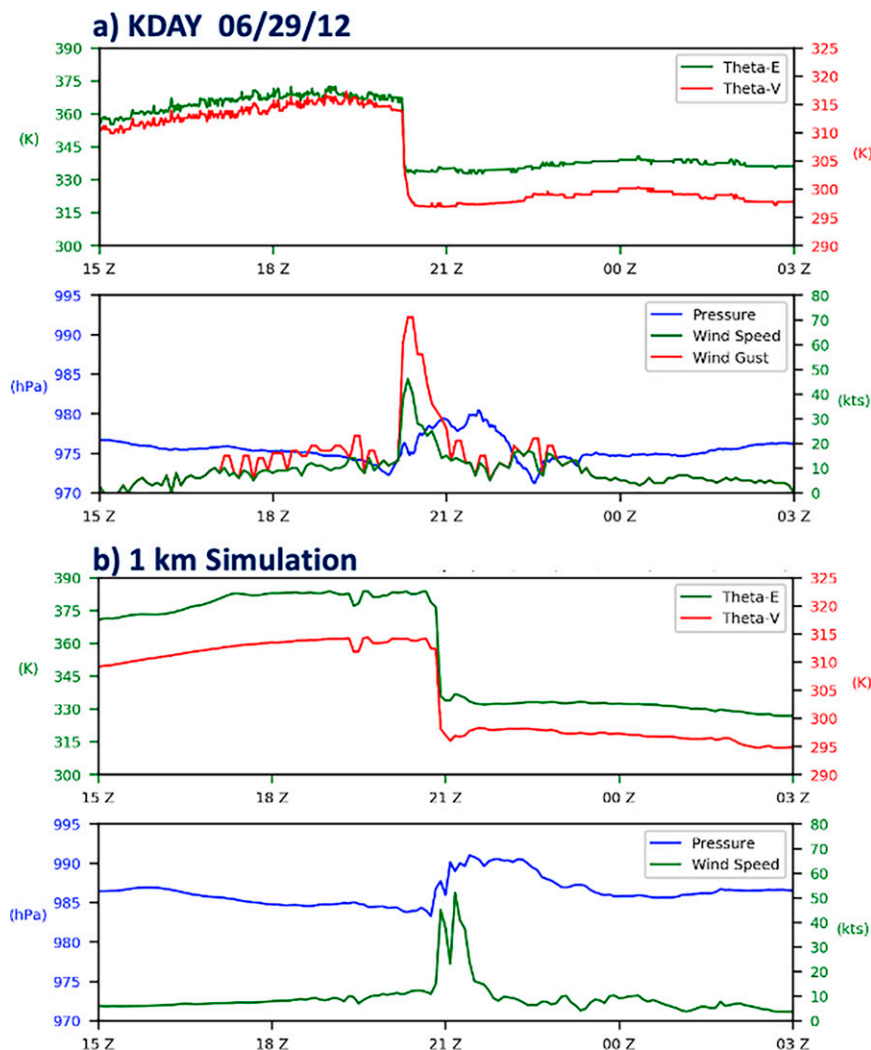


FIG. 8. Time series of surface θ_v (K) and θ_e (K), pressure (hPa), wind speed (kt), and wind gusts (kt) (a) as observed at Dayton, OH, on 29 Jun 2012 and (b) as diagnosed from the 1-km simulation at the equivalent location.

e. Surface wind characteristics

Severe surface winds within QLCs can be generated by a variety of mechanisms, ranging from most simply developing in a strong mean surface wind environment, to being generated by the accelerations associated with convective and mesoscale downdrafts and associated cold pools, as well as accelerations associated with the development of mesoscale vortices. Such vortices may be associated with supercells embedded within the convective system, but often develop in association with nonsupercellular features, such as bow echoes, LEWPs, etc. (e.g., Trapp and Weisman 2003; Weisman and Trapp 2003; Wakimoto et al. 2006). The most severe winds, however, are often the result of the additive contributions from all these forcing influences. Thus, the ability to predict severe surface winds in such

systems depends critically on the ability to resolve these forcing features.

In the following, observed maximum surface winds were documented using both the available 5-min ASOS time series, within a roughly 20-min time period after documented gust front passage (as described in section 2c), as well as National Weather Service (NWS) storm reports. The NWS storm reports were especially helpful given the inherent local nature of severe wind gusts, and the relative sparsity of ASOS reports at times. However, the ASOS observations alone were used for direct comparison with the model results, given the inherent uncertainties in the accuracy of the storm reports at times. Simulated maximum surface winds were similarly diagnosed using the maximum 10 m AGL winds from the 5-min time series. Comparison with the observed maximum winds is compromised somewhat by the lack of gust information from the simulations.

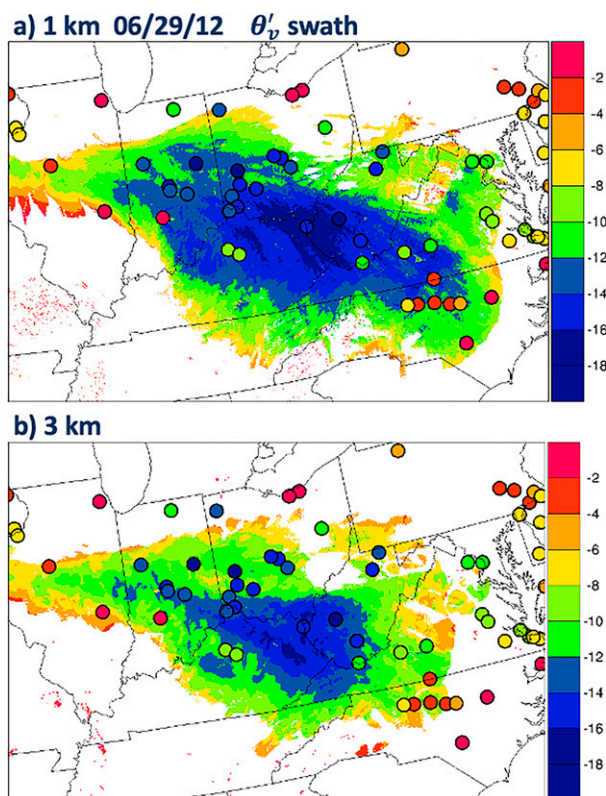


FIG. 9. Swaths of maximum θ_p' (shading; K) for 29 Jun 2012, for the (a) 1- and (b) 3-km WRF-ARW simulations, as described in the text. Colored dots represent the equivalent maximum observed θ_p' for all available ASOS stations for this case.

3. Case overviews

The 14 QLCS cases selected for this study (Table 1) all evolved in a classic fashion for such convective systems, developing a leading line trailing stratiform reflectivity structure during their mature phases, with embedded bow echo and/or LEWPs evident at times, as are often associated with the production of the most severe weather within such systems. The mature system reflectivity structure for the 27 April 2011, 29 June 2012, 26 April 2016, and the 30 June 2014 cases are presented in Fig. 1, and are representative of the range of reflectivity characteristics observed with the full set of events. The severe weather associated with these events, as reported by the Storm Prediction Center (SPC), is shown in Fig. 2. Of these four cases, bowing or LEWP structures were most evident in the 27 April 2011 case (Fig. 1a), and were associated with a significant outbreak of QLCS tornadoes in Alabama during the early morning hours (e.g., Knupp et al. 2014). One particularly well-formed bowing feature is also evident within the 30 June 2014 convective system (Fig. 1c) and was associated with an extensive swath of damaging surface winds in eastern Iowa, along with one confirmed tornado.

Figure 3 presents the basic environmental conditions for these four cases, including 500-hPa heights, most-unstable convective available potential energy (CAPE) and 0–6-km AGL

vertical wind shear, as representative of the time being portrayed for each case, as taken from the 1-km simulations (the differences in environmental characteristics between the 1- versus 3-km environments were not found to be significant). As also noted for the full set of 14 cases (Table 1), these four cases cover a wide range of environments spanning from extreme CAPE with weak vertical wind shear and weak synoptic scale forcing for the 29 June 2012 derecho (Fig. 3b), to more modest CAPE with strong shear and stronger synoptic scale forcing for the 27 April 2011 event (Fig. 3a).

Figures 4a and 4b through 7a and 7b depict the mature simulated reflectivity structure at 1 and 3 km for each of the four selected cases. As has been noted in many past studies using CAMs, some errors in timing and location are apparent in comparison to the observed systems (Fig. 1). For the present set of cases, the timing and location of convective initiation is very similar in the 1- and 3-km simulations. The forecasts for the 27 April 2011 case are shifted a bit north of the observed system using both 1 and 3 km. This is a relatively common mode of forecast failure for this model setup (seen in 5 of the 14 cases), and work is ongoing to understand this bias. However, the overall morphology of these and the other nine events included in the present study (Table 1) are reproduced quite reasonably. Still, some systematic differences are evident in comparing the 1- and 3-km forecasts, with the 1-km forecasts often depicting a more realistic leading-line trailing-stratiform reflectivity structure, slightly faster propagation, and more numerous smaller scale LEWPs evident along the leading edge of the system. In the following, we will discuss some of the more detailed characteristic associated with the production of severe weather, including cold pool structure and strength and the production of leading-line and line-end vortices, both of which contribute to the production of severe surface winds and potential QLCS tornadoes.

4. Cold pool characteristics

As noted above, cold pools represent one of the critical components distinguishing QLCSs from less organized forms of convection, contributing to their maintenance, propagation, and severe weather potential. In this section, we offer a more detailed presentation of the impact of resolution on cold pool and outflow production for our set of simulations and attempt to validate these system characteristics using surface observations.

Some of the basic differences in cold pool characteristics for the 1- and 3-km simulations are apparent in Figs. 4c and 4d through 7c and 7d, which depict surface θ_p for the four sample cases described above during their mature phase. In general, the cold pools are slightly colder and larger at 1 versus 3 km. The only exception among these four sample cases is perhaps 30 June 2014 (e.g., Figs. 6c,d), which, at the analysis time, only depicts an enhanced cold pool for the 1-km simulation in a narrow strip just behind the active convective line in east-central Iowa. However, the 1-km cold pool does clearly become stronger and larger than the 3-km cold pool at later times in the simulation (not shown). All in all, the stronger 1-km cold pools are consistent with the slight

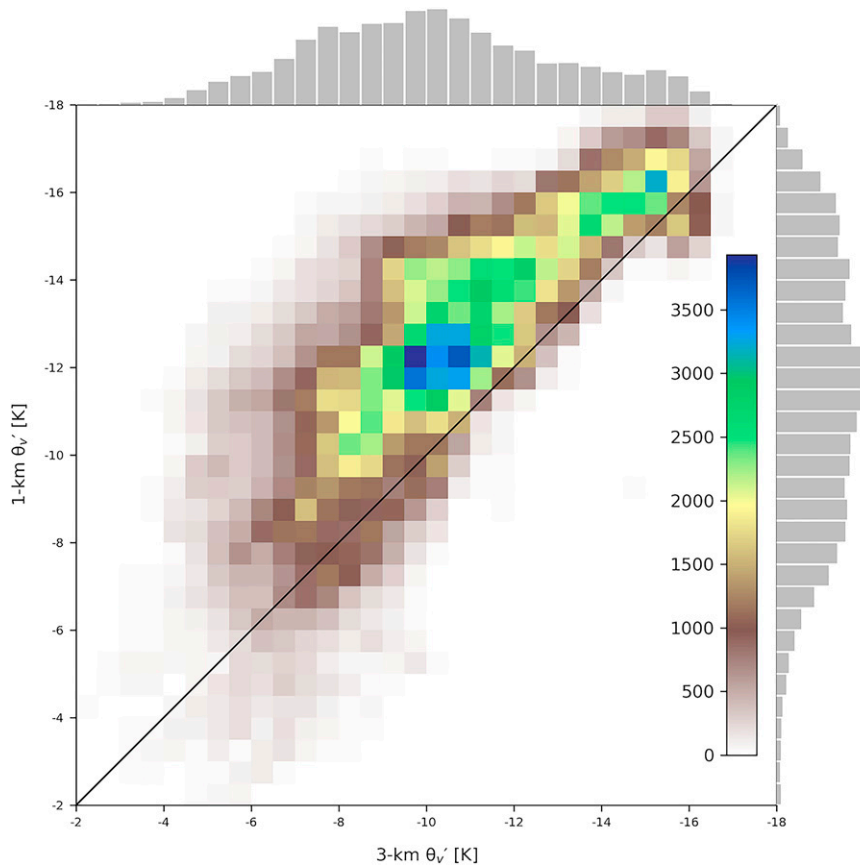


FIG. 10. 2D histogram of θ_v (K) for 29 Jun 2012, for the 1- vs 3-km WRF-ARW simulations. For this purpose, 3-km gridpoint magnitudes were interpolated to 1-km grid points. Points are included only where the 1- and 3-km cold pool swaths overlap. The 1D histograms of the 3- and 1-km swaths are shown along the top and right borders, respectively.

increase in propagation speed for the 1-km simulations, as noted above and in previous studies (e.g., Schwartz et al. 2017; Squitieri and Gallus 2020).

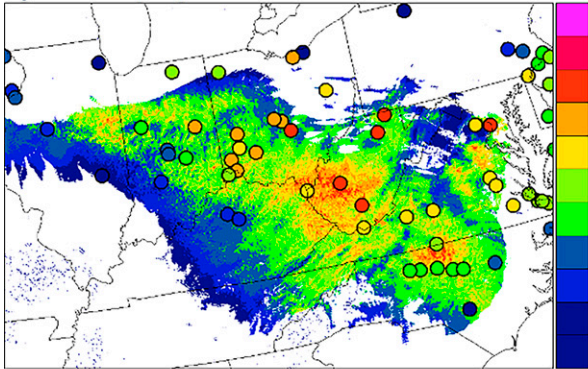
The 29 June 2012 event represents an extreme example of such cold pool generation. Figure 8a shows the observed time series of surface observations from Dayton, Ohio, showing a 17-K drop in potential temperature and a 40-K drop in θ_e along with a 7–8-hPa pressure rise as the cold pool passes by. Model time series for Dayton from the 1-km simulation is presented in Fig. 8b, showing similar magnitudes for θ_v and ΔP .

Figure 9 documents the maximum cold pool generated θ_v , as observed from available ASOS stations on this day, overlaid with the equivalent parameters from the 1- and 3-km simulations. The θ_v values of 12–16 K are evident all along the system's path, both for the observations and simulations. However, as also noted above (e.g., Fig. 5), the 1-km cold pool swath is larger and, on average, colder than the 3-km swath. These differences in cold pool θ_v characteristics are documented further in histogram format (Fig. 10), which shows the 1-km simulation producing colder θ_v values on a point-by-point basis over most of the system's swath.

Figures 11 and 12 document the maximum cold pool generated ΔP and minimum θ_e , respectively, as observed from available ASOS stations on this day, again overlaid with the equivalent parameters from the 1- and 3-km simulations. A ΔP value of 6–8 hPa, and minimum values of θ_e near 330 K were observed all along the system's path.

Although the simulated systems were slightly south of the observed system on this day, both the 1- and 3-km simulations successfully reproduced the observed range of surface conditions. However, the size and speed of propagation of the cold pool is clearly a bit larger for the 1-km case, which also exhibits a 2–3 K larger θ_v than the 3-km simulation.

The results for all 14 cases are summarized in Figs. 13–16, which compare the observed event cold pool characteristics (θ_v , ΔP , θ_e) to the analogous event characteristics generated in the 1- and 3-km simulations. For this purpose, representative values of each parameter were chosen from the most intense phase of each system, as determined from the individual θ_v , ΔP , θ_e event swaths and 2D histograms, as presented in Figs. 9 through 12 above for the 29 June 2012 event. The representative maximum θ_v values (Fig. 13) ranged from –4 to –16 K for the 14 cases, producing a reasonably representative

a) 1 km 06/29/12 ΔP swath

b) 3 km

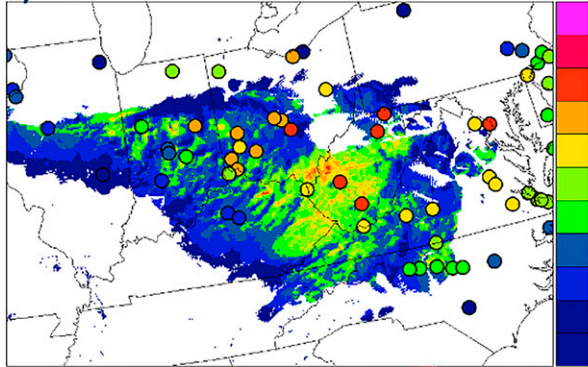
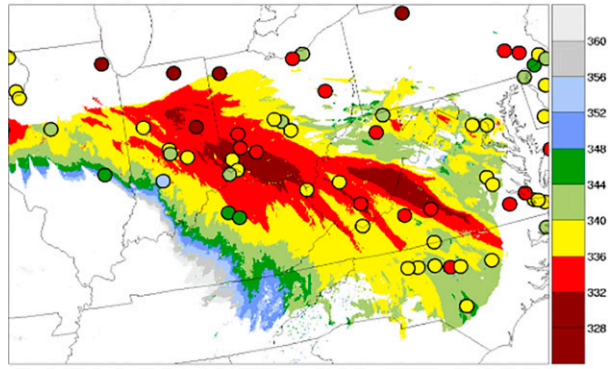


FIG. 11. Swaths of maximum perturbation surface ΔP (hPa) (shading) for 29 Jun 2012, for the (a) 1- and (b) 3-km WRF-ARW simulations, as described in the text. Colored dots represent the equivalent maximum observed ΔP for all available ASOS stations for this case.

set of cold pool strengths (e.g., Engerer et al. 2008). Both the 1- and 3-km simulated $-\theta'_v$ reasonably reproduce the range and magnitude of the observed cold pools, within ± 2 K. Generally, the 1-km simulated cold pools are consistently cooler than the 3-km cold pools, as was also noted in Schwartz et al. (2017). Again, this result is further documented via a 2D histogram, aggregated over all 14 cases (Fig. 14), which generally shows the 1-km simulations being colder for the stronger cold pool cases with θ'_v values greater than -7 K. However, for the weaker cold pool cases, the 3-km simulations seemed slightly colder than the 1-km simulations.

Figure 15 similarly presents the maximum event ΔP observed and simulated for all 14 cases. ΔP magnitudes range from 2 to 8 hPa over this set of cases, and the modeled and observed ΔP generally display good correspondence, $\pm \sim 1$ hPa, with the one exception from 13 July 2015. Indeed, assuming an average cold pool θ'_v ranging between 2 and 8 K from case to case, and assuming an average cold pool depth of 3.5 km, the expected hydrostatic ΔP would range between 2 and 8 hPa, respectively, which reflects the strong relationship between these two parameters in Figs. 13 and 15. However, no clear distinctions arise when comparing the 1- and 3-km simulations for this parameter.

a) 1 km 06/29/12 θ_e swath

b) 3 km

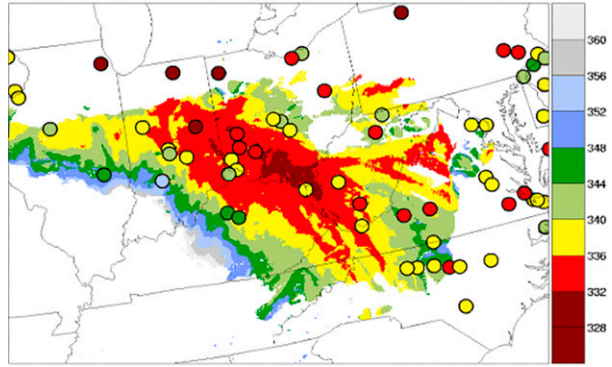


FIG. 12. Swaths of cold pool generated surface θ_e (shading; K) for 29 Jun 2012, for the (a) 1- and (b) 3-km WRF-ARW simulations, as described in the text. Colored dots represent the equivalent observed θ_e for all available ASOS stations for this case.

Figure 16 shows results for surface θ_e , again suggesting that the simulations successfully reproduced the observed range of cold pool θ_e . However, there is now a consistent slight cold bias as compared to the observed θ_e for both the 1- and 3-km simulations. Since the cold pool θ_e is often representative of the midlevel origin of the downdraft/cold pool air mass, this suggests that the environmental midlevel θ_e is either a bit too low, or that the source level for the downdraft air mass is misrepresented in this set of simulations, perhaps due to initialization or other model errors. A comparison of the observed and modeled environmental θ_e (not shown), however, did not suggest any systematic error in the modeled environmental midlevel θ_e . Additionally, an inspection of the vertical gradients of θ_e at midlevels suggests that a couple of degree difference in the simulated θ_e would not suggest a significant change in the height of origin of the downdraft air mass. Thus, the apparent slight cold bias in cold pool θ_e for this set of simulations is not considered to be significant.

5. Mesoscale vortices

Figures 17–20 compare the low-level wind, updraft, vertical vorticity structure, and UH01 tracks for the 29 June 2012, 30 June 2014, 27 April 2011, and 27 April 2016 cases at 1 and 3 km. Based on the associated reflectivity characteristics, the

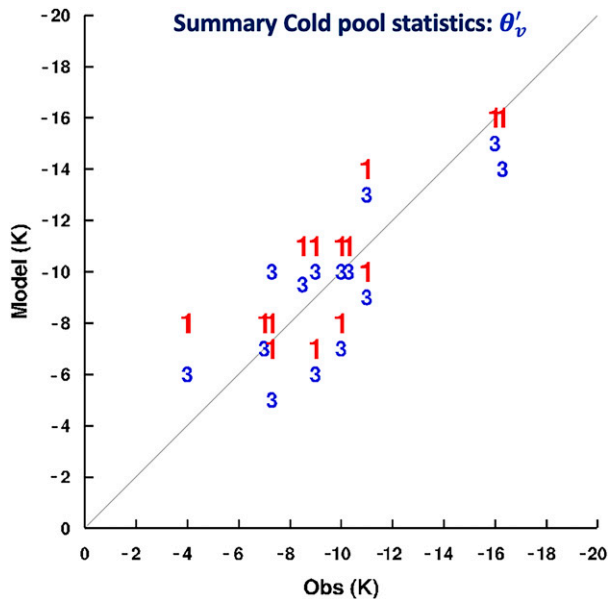


FIG. 13. Simulated vs observed maximum surface θ'_v for all 14 cases, as described in the text. The 1-km simulation results are depicted with red “1” labels, and the 3-km results are depicted with the blue “3” labels. Some of cases have been shifted slightly on the observational axis to better distinguish among cases with equivalent observed θ'_v .

overall character of the observed vortices for these cases seems to be reasonably represented by the simulations. However, while both resolutions seem capable of producing larger mesoscale vortices, the 1-km simulations appear generally more apt to produce smaller-scale vortices along the system’s leading line, as can be identified by narrow streaks of large UH01 magnitudes (Figs. 17b, 18b, 19b, and 20b).

The 29 June 2012 case is representative of cold pool dominated events that occur in environments of very large CAPE but weak deep layer shear (Fig. 17). Although embedded supercells and other deep mesoscale vortices would not be expected in such environments, shallow mesoscale vortices still occur along the leading edge of such systems, as is especially evident in the 1-km simulation (Fig. 17b). However, these shallow vortices tend not to be as associated with significant local enhancements of the outflow winds, as can occur with the deeper embedded mesoscale vortices. Likewise, QLCS tornadoes tend to be very rare with such systems, and indeed, despite the large extent of severe outflow winds, no such tornadoes were reported with this case.

The 30 June 2014 case (Fig. 18) is characteristic of stronger shear events, with the 0–6-km AGL environmental vertical wind shear magnitude ranging between 40 and 50 kt. Such magnitudes of vertical wind shear are generally sufficient to produce embedded supercells as well as the nonsupercellular mesoscale vortices. Deep, embedded mesoscale vortices are evident in both the 1- and 3-km simulations, associated with LEWP type reflectivity features (e.g., Fig. 6), and, similar to the 29 June case, additional smaller-scale vortices

appear in the 1-km simulation. These vortices are also clearly coincident with long-lived UH01 tracks, suggesting that embedded supercells may have contributed to mesoscale vortex formation in this case (a tornado was observed with this event). Although the 1-km simulation again produces more smaller vortices, the singular large and strong mesoscale vortex evident in the equivalent 3-km simulation seems more consistent with the observations on this day (e.g., note the singular LEWP reflectivity structure in Fig. 1c).

The 27 April 2011 case (Fig. 19) represents another strong shear event that was especially notable in that the early morning QLCS produced an extensive number of tornadoes associated with both leading line and line-end mesoscale vortex structures (e.g., Knupp et al. 2014). The 1-km simulation produces both a larger-scale embedded mesoscale vortex along the Alabama–Tennessee border, as well as a series of smaller-scale vortices along the leading edge of the system extending south from this larger-scale vortex, as identified by the several narrow UH01 streaks (Fig. 19b). Wide swaths of significant UH01 are also evident extending from the leading edge of both the 1- and 3-km simulations. However, for this case, these features simply reflect the more general 2D correlation of low-level updraft and cyclonic vorticity along the entire edge of the system as opposed to the more isolated mesoscale vortices generally associated with enhanced severe weather and possible tornadoes.

Finally, the 26 April 2016 case (Fig. 20) is quite representative of a moderate shear case, producing more linear reflectivity segments as opposed to more isolated supercell-type configurations, and also producing a fair number of QLCS-type tornadoes, primarily in northeast Oklahoma. Again, although the potentially severe segment in the simulations was a bit further south than the observed system, the 1-km simulation produced several intense low-level updraft helicity tracks embedded with the bow shaped reflectivity features. However, as for the 27 April 2011 case (Fig. 19), only a single larger updraft helicity track is evident in the 3-km simulation, extending along the center of a bow shaped reflectivity segment. Again, this feature seemed more associated with the collocation of low-level cyclonic shear and updraft at the leading of the system, as opposed to the development of a localized vortex that might be associated with enhanced severe weather. For the present case, the existence of multiple QLCS-type tornadoes associated with the observed system would seem to better support the guidance offered by the 1-km simulation.

6. Surface winds

The variety of maximum surface wind patterns for the present set of QLCSs is illustrated in Fig. 21, which depicts 1-h maximum wind swaths during the mature phases of the 29 June 2012, 30 June 2014, and 27 April 2011 cases, as also discussed above. The 29 June 2012 case was the most extensive severe surface wind event of the cases considered herein, with observed wind gusts of 50–70 kt and local maximum wind gusts up to 90 kt in the NWS severe weather reports (Fig. 2b) through much of the system’s path, especially through Ohio and West Virginia. For this case, the primary forcing for the

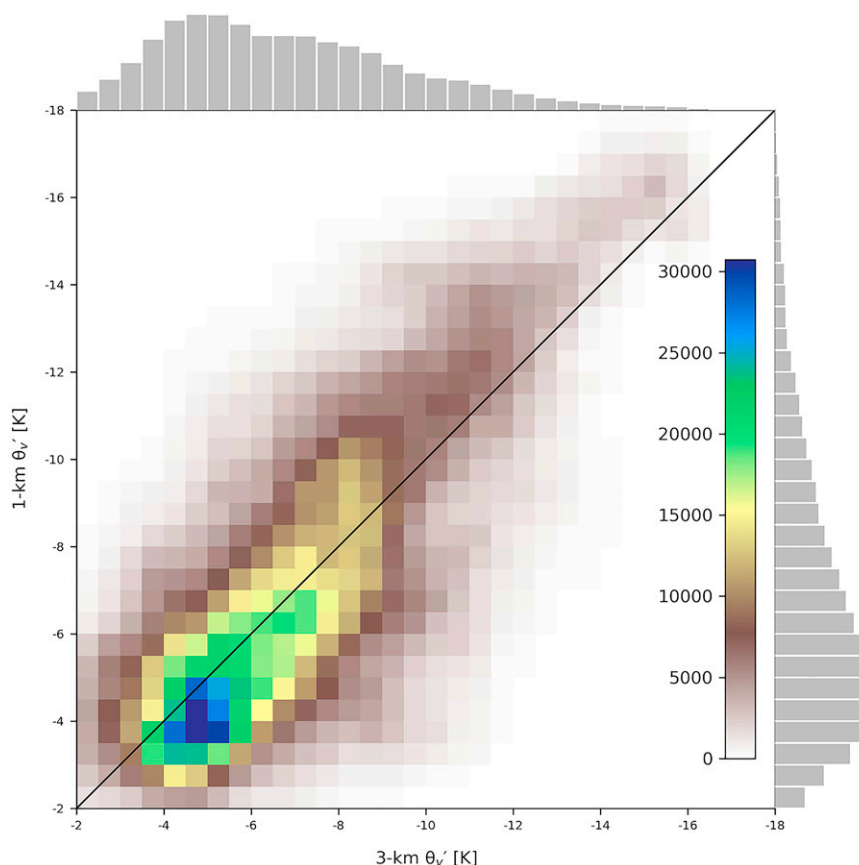


FIG. 14. The 2D histogram of θ'_v (K) for the 1- vs 3-km WRF-ARW simulations, aggregated over all 14 cases. For this purpose, 3-km gridpoint magnitudes were interpolated to 1-km grid points. Points are included only where the 1- and 3-km cold pool swaths overlap. 1D histograms of the 3- and 1-km swaths are shown along the top and right borders, respectively.

severe surface winds was the intense cold pool and associated rear-inflow jet, with perhaps some local enhancement from small, shallow embedded vortices along its leading edge. The 1-km simulation produced a larger cold pool in this case, as noted above, along with more shallow leading line embedded vortices, but both the 1- and 3-km simulations produced similar strength cold pools and rear-inflow jets. Overall, the 1-km simulation produced slightly stronger surface winds.

The 30 June 2014 system (Figs. 21c,d) also produced widespread observed maximum wind gusts up to 60 kt extending across southern Iowa and north central Illinois, with locally extreme winds up to 90 mph, specifically in association with an embedded bow echo and an apparent associated mesoscale vortex on the Iowa–Illinois border. For this case, the 1-km simulation produced a more extensive region of strong surface winds than the 3-km simulation, consistent with a more extensive and slightly colder cold pool. The 1-km simulation also produced more narrow swaths of enhanced surface winds, largely associated with its more numerous embedded leading line mesoscale vortices (as also depicted by its more numerous UH swaths in Fig. 18). Most notably, though, the strongest simulated surface winds for this case, reaching over

90 kt, were generated in the 3-km simulation, which produced a larger and more coherent swath of high winds associated with a single, large embedded mesoscale vortex associated with a bulge in the reflectivity field, similar to what was observed on this day (e.g., Fig. 1c). This case emphasizes that, although the 1-km simulations seem to consistently produce more embedded mesoscale vortices, 3-km simulations are capable of producing large mesoscale vortices that significantly enhance surface winds under the right environmental conditions.

For the 27 April 2011 case (Figs. 22e,f), the 1-km simulation produces generally stronger and more extensive surface outflow associated with the cold pool as well as more intense narrow swaths of strong surface winds associated with embedded mesoscale vortices, which are largely absent in the 3-km simulation. As such, the 1-km simulation is more accurate in representing the potential for severe surface winds as well as the multiple QLCS tornadoes that were observed for this case. Interestingly, the strongest surface winds in the 1-km simulation were again associated with both a large mesoscale vortex as well as smaller leading-line vortices, although the larger mesoscale vortex was not clearly identified as an enhanced swath of UH.

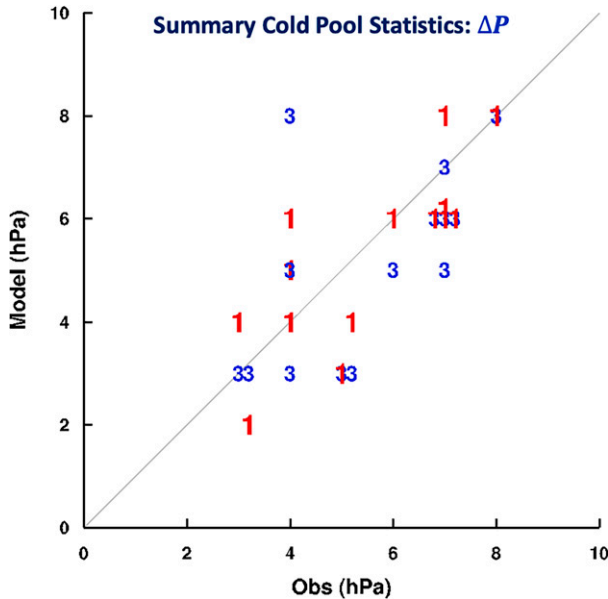


FIG. 15. Simulated vs observed cold pool surface pressure change, ΔP (hPa), for all 14 cases, as described in the text. The 1-km simulation results are depicted with red “1” labels, and the 3-km results are depicted with blue “3” labels. Some of the cases have been shifted slightly on the observational axis to better distinguish among cases with equivalent observed ΔP .

The maximum surface wind characteristics for all 14 cases is presented in Fig. 22. While there is certainly some correspondence between the simulated and observed maximum winds over all the cases, the correlation does not seem as strong as for the cold pool characteristics (e.g., Figs. 13–16). This is likely because, as discussed above, the embedded mesoscale vortices can also be a significant contributor to surface wind strength. Also, while the surface wind strength is consistently stronger for the 1- versus 3-km simulations, the 3-km simulations appear to match the observed winds a bit better.

7. Summary, discussion, and conclusions

Herein, we have compared the structure of 14 simulated severe QLCS using 1- and 3-km grid spacings, to better document the capabilities of these resolutions to represent the phenomena often associated with the production of hazardous weather within such systems. This study represents an extension of a similar study by Squitieri and Gallus (2020) to consider events over a wider range of environmental conditions, and to better validate the more detailed system features associated with severe weather production. As such, emphasis is placed on documenting overall reflectivity characteristics, objectively validating cold pool characteristics as compared to the observations, and documenting low-level mesovortex and surface wind characteristics, which were not included in this previous study.

As to the overall reflectivity characteristics, the basic leading-line trailing stratiform structure that is commonly observed with mature QLCSs was often better defined at 1 versus 3 km.

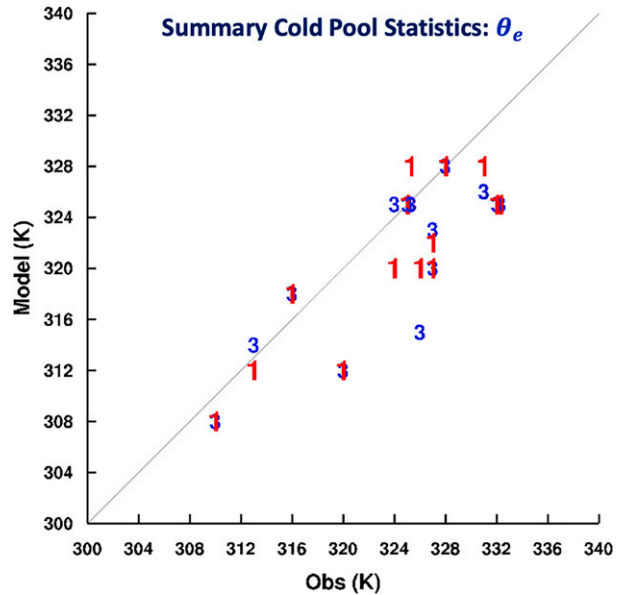


FIG. 16. Simulated vs observed minimum cold pool surface θ_e for all 14 cases, as described in the text. The 1-km simulation results are depicted with red “1” labels, and the 3-km results are depicted with the blue “3” labels.

This result is consistent with many recent studies that find that reflectivity features are better represented using enhanced resolution (e.g., Bryan et al. 2003; Kain et al. 2008; Schwartz et al. 2009; Bryan and Morrison 2012; Schwartz et al. 2017). Additionally, while 3-km grid spacing seems sufficient to reproduce LEWP and bow echo type configurations embedded within larger QLCSs, such features seem more numerous, and are generally of smaller scale using 1-km grid resolutions. The enhanced ability to produce such LEWP type features using 1-km grid spacing did improve the forecast guidance for some cases (e.g., the 27 April 2011 and 27 April 2016 cases). However, it was not as clear whether the enhanced grid resolution, considering the full set of 14 cases, provided a significant improvement more generally in the representation of such reflectivity features.

In comparing the cold pool characteristics, both the 1- and 3-km simulations well replicated the basic variations observed for the differing environments from case to case. As has also been noted in previous studies (e.g., Schwartz et al. 2017; Squitieri and Gallus 2020), the 1-km cold pools were generally slightly colder, larger in area, and slightly faster than those of the 3-km systems. However, for the present set of cases, the peak intensity displayed by the simulated 3-km cold pools seemed a bit more consistent with the observations. More generally, simulated cold pool pressure changes were generally a bit larger than the observed pressure changes, for both resolutions. Also, the simulated cold pool θ_e was consistently slightly lower than observed, perhaps indicating drier simulated midlevel environmental conditions than observed.

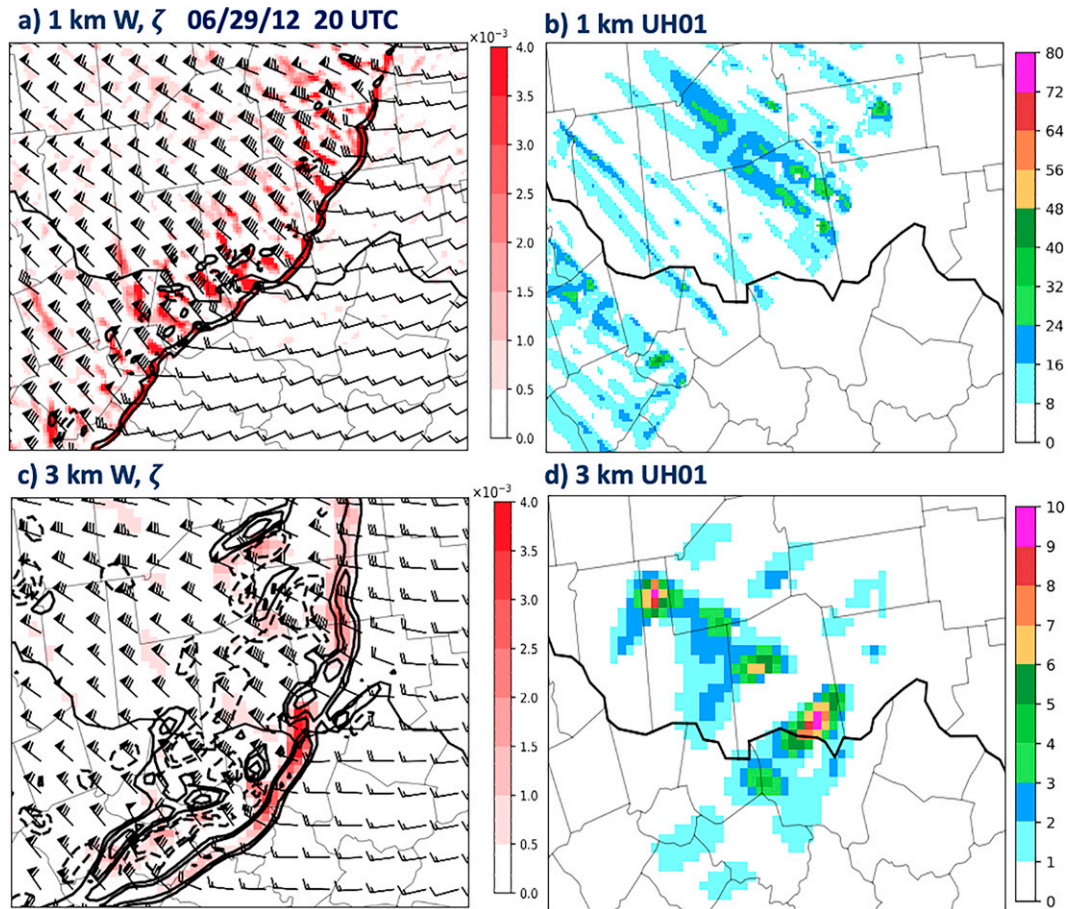


FIG. 17. (a),(c) The 925-hPa winds (kt), 1-km vertical velocities (W ; contours for 3 km: $-4, -2, -1, 1, 2, 4 \text{ m s}^{-1}$; contours at 1 km: $-15, -10, -5, 5, 10, 15 \text{ m s}^{-1}$; negative values dashed), and positive vertical vorticity (ζ ; s^{-1} ; shading); and (b),(d) 0–1-km 1-h maximum updraft helicity swaths (UH01; $\text{m}^2 \text{s}^{-2}$; shading) for 1- and 3-km simulations at 2000 and 2100 UTC, respectively, for 29 Jun 2012. Wind bars are spaced every 10 km.

Both the 1- and 3-km simulations were successful in producing embedded low-level mesoscale vortices within the convective systems, although these vortices were generally smaller in scale and more numerous using the 1-km grid. While these vortices using 1-km resolutions generally better matched the observations, in some cases (e.g., 30 June 2014) the scale and number of mesoscale vortices in the 3-km simulations seemed better aligned with the observations. The ability of 3-km simulations to realistically reproduce such larger mesoscale vortices was also highlighted for the 8 May 2009 super derecho event wherein the northern line-end mesoscale vortex developed a warm-core structure along with hurricane force surface winds (e.g., Weisman et al. 2013). However, although many leading-line vortices and subsequent tornadoes were observed with this system, the 3-km forecast produced only a solid band of positive vertical vorticity extending along the gust front, similar to the 3-km simulation of the 27 April 2011 case presented herein. It is also important to note that, while UH01 was quite effective in identifying many of these QLCS mesoscale vortices, some of the mesoscale vortices that contributed to the production of severe

winds in the simulations were not collocated with updrafts (e.g., 27 April 2011). Likewise, continuous wide swaths of high UH01 were generated along the leading line of some of the convective systems. However, such features were found to be quite shallow, and were not indicative of the same level of severe weather risk attributed to supercells. Thus, caution must be used when applying UH concepts to QLCS mesoscale vortices.

Simulated convective surface wind strength was related to both the strength of the resulting convective cold pools as well as the occurrence of low-level mesoscale vortices embedded within the leading line of the system, making the predictability of such system attributes more complicated. The inherent difficulty in documenting such small-scale phenomena like wind gusts, especially given the sparsity of surface wind observations at times, makes validating surface winds even more difficult. Indeed, maximum surface winds were only marginally well predicted for the 14 cases. The simulations, however, were able to differentiate the potential mechanisms contributing to severe winds from case to case. For instance, the widespread extreme winds on 30 June 2012 were clearly produced

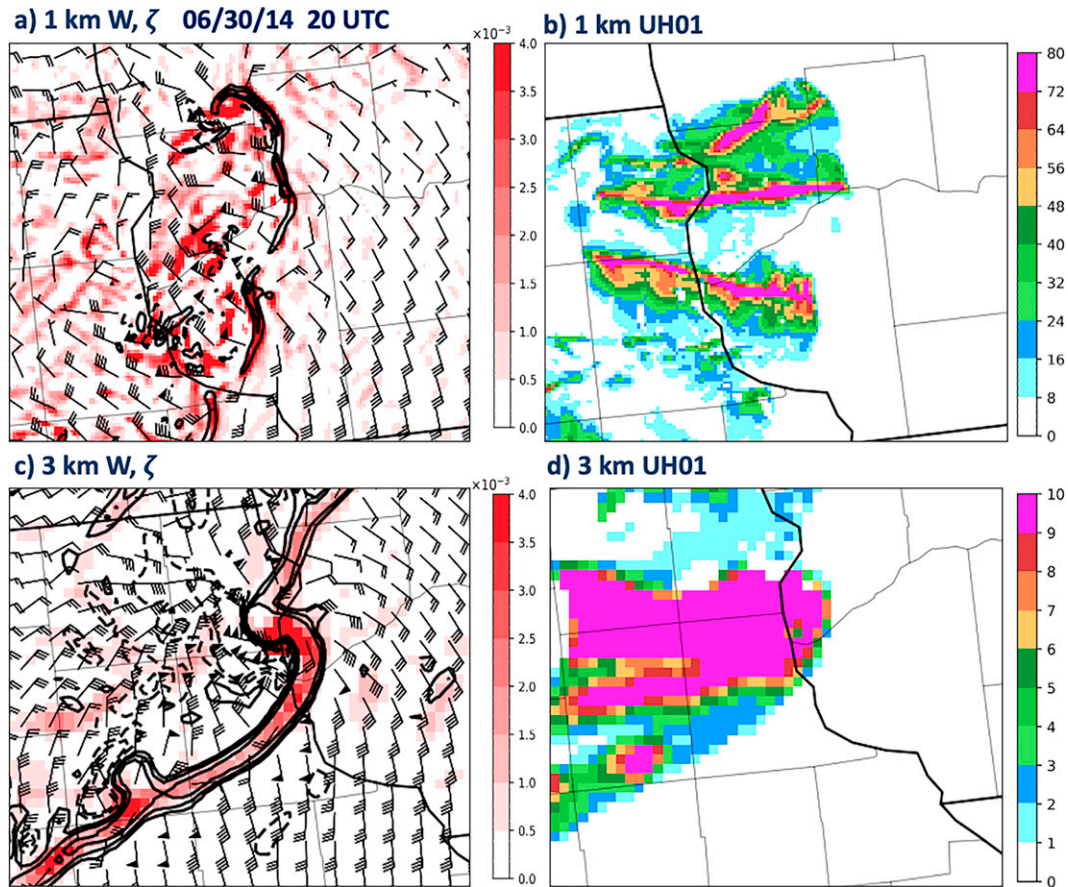


FIG. 18. (a),(c) The 925-hPa winds (kt), 1-km vertical velocities (W ; contours for 3 km: $-4, -2, -1, 1, 2, 4 \text{ m s}^{-1}$; contours for 1 km: $-15, -10, -5, 5, 10, 15 \text{ m s}^{-1}$; negative values dashed), and positive vertical vorticity (ζ ; s^{-1} ; shading); and (b),(d) 0–1-km 1-h maximum updraft helicity swaths (UH01; $\text{m}^2 \text{s}^{-2}$; shading) for 1- and 3-km simulations, respectively, for 2000 UTC 30 Jun 2014. Wind barbs are spaced every 10 km.

by an especially intense cold pool, while the production of locally extreme winds on 27 April 2011 and 30 June 2014 were more associated with embedded mesoscale vortices. Interestingly, while the 1-km systems generally produced stronger surface winds than the 3-km systems, the 3-km winds seemed a bit more accurate.

The overall results presented here are quite consistent with the previous related studies, suggesting that some improvement in convective system structure and potential hazard prediction is achieved by increasing the grid resolutions from 3 to 1 km, especially in the ability of the 1-km simulations to produce more realistic reflectivity features as well as the smaller, often more realistic leading-line vortices that can be associated with QLCS tornadoes. However, whether such improvements are significant enough to warrant operational resolution increases to represent QLCS type phenomena is still an open question. This, of course, depends strongly on the forecast perspective being taken. While such improvements may not be necessary for longer-term forecasts (e.g., $>24 \text{ h}$), a better representation of convective

system-scale properties and explicit hazard potential might be considered critical for shorter-term warning applications.

Acknowledgments. This work was partially supported by NOAA OAR Grant NA17OAR4590182 and the NCAR Short-term Explicit Prediction (STEP) program. We thank Joseph Klemp (NCAR/MMM) for an internal review and three anonymous reviewers for comments that improved the paper. We would also like to acknowledge high-performance computing support from Cheyenne (Computational and Information Systems Laboratory 2017) provided by NCAR's Computational and Information Systems Laboratory. The National Center for Atmospheric Research is sponsored by the National Science Foundation.

Data availability statement. The output from our 14 corresponding 3- and 1-km numerical forecasts are available from the corresponding author. ASOS surface observations were obtained from <https://mesonet.agron.iastate.edu/ASOS/>.

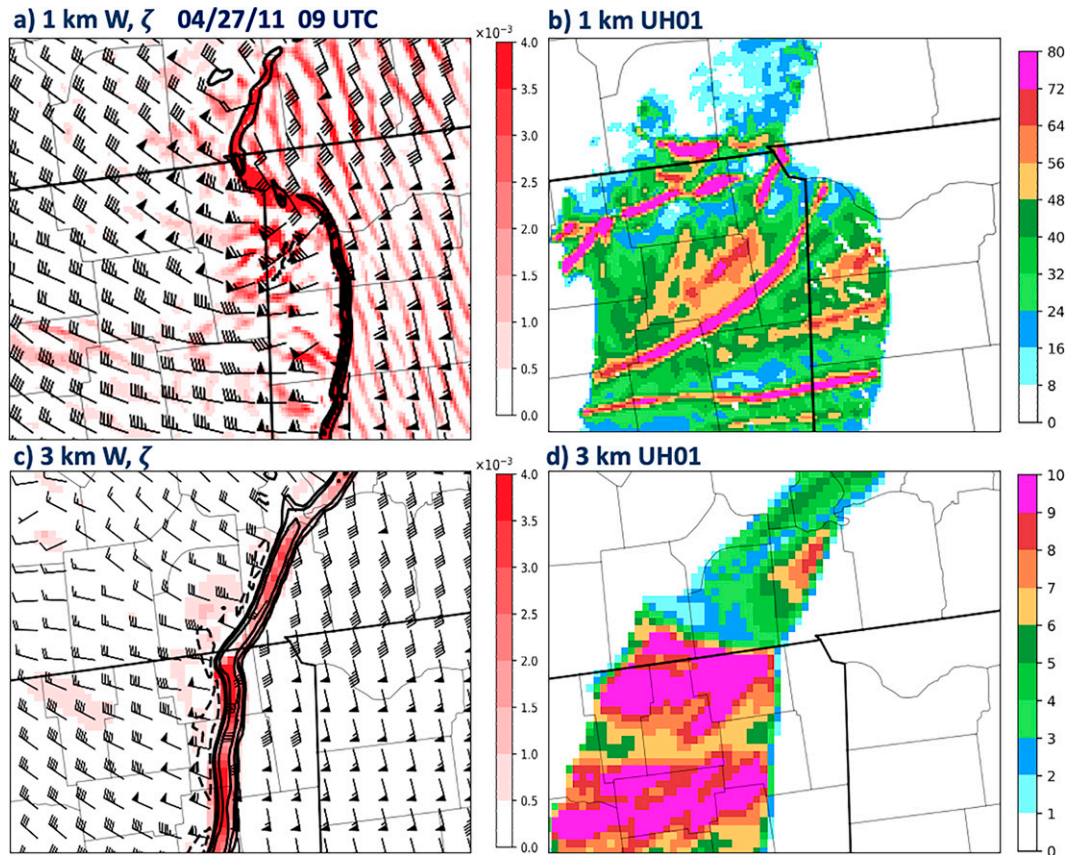


FIG. 19. (a),(c) The 925-hPa winds (kt), 1-km vertical velocities (W ; contours for 3 km: -4 , -2 , -1 , 1 , 2 , 4 $m s^{-1}$; contours for 1 km: -15 , -10 , -5 , 5 , 10 , 15 $m s^{-1}$; negative values dashed), and positive vertical vorticity (ζ ; s^{-1} ; shading); and (b),(d) 0-1-km 1-h maximum updraft helicity swaths (UH01; $m^2 s^{-2}$; shading) for 1- and 3-km simulations, respectively, for 0900 UTC 27 Apr 2011. Wind barbs are spaced every 10 km.

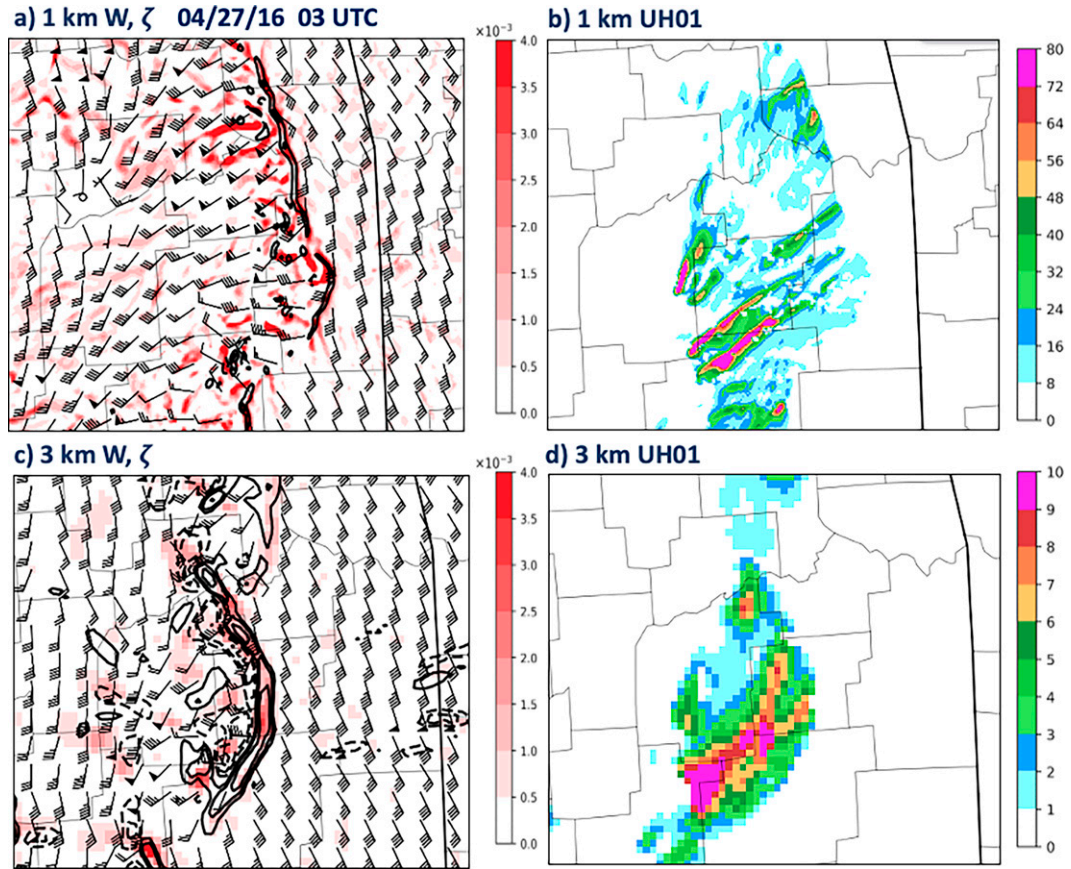


FIG. 20. (a),(c) The 925-hPa winds (kt), 1-km vertical velocities (W ; contours for 3 km: $-4, -2, -1, 1, 2, 4 \text{ m s}^{-1}$; contours for 1 km: $-15, -10, -5, 5, 10, 15 \text{ m s}^{-1}$; negative values dashed), and positive vertical vorticity (ζ ; s^{-1} ; shading); and (b),(d) 0–1-km 1-h maximum updraft helicity swaths (UH01; $\text{m}^2 \text{s}^{-2}$; shading) for 1- and 3-km simulations, respectively, for 0300 UTC 27 Apr 2016. Wind barbs are spaced every 10 km.

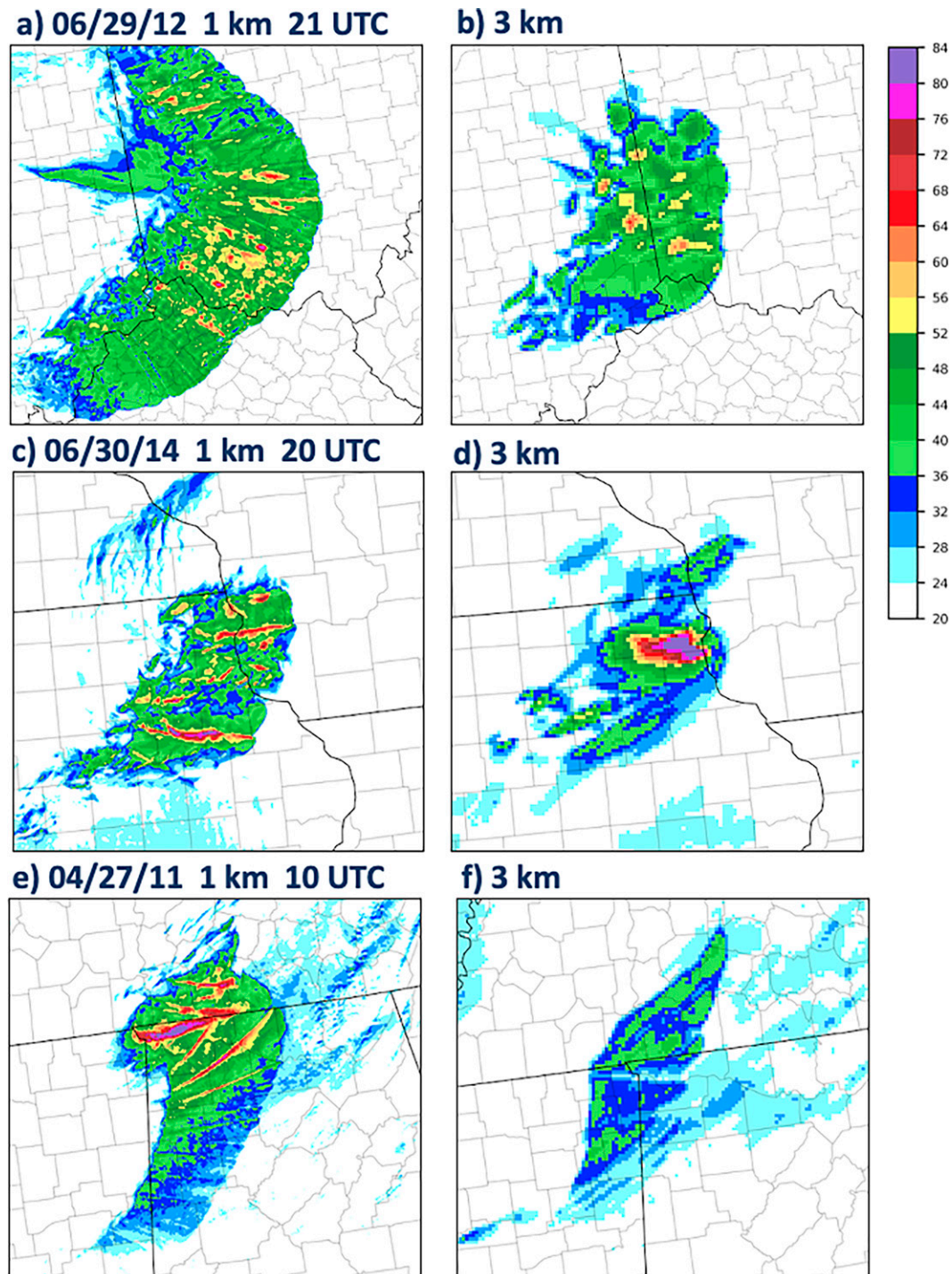


FIG. 21. The 1-h maximum surface winds swath (kt) from 1- and 3-km simulations for (a),(b) 2100 UTC 29 Jun 2012; (c),(d) 2000 UTC 30 Jun 2014; and (e),(f) 1000 UTC 27 Apr 2011.

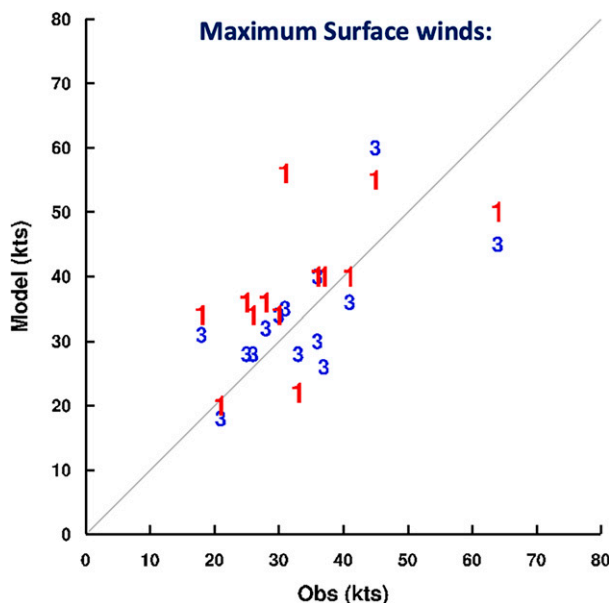


FIG. 22. Simulated vs observed maximum surface wind gusts (kt) for all 14 cases, as described in the text. The 1-km simulation results are depicted with red “1” labels, and the 3-km results are depicted with blue “3” labels. Some of the cases have been shifted slightly on the observational axis to better distinguish among cases with equivalent observed wind speed.

REFERENCES

- Adlerman, E. J., and K. K. Droegemeier, 2002: The dependence of numerically simulated cyclic mesocyclogenesis to variations in model physical and computational parameters. *Mon. Wea. Rev.*, **130**, 2671–2691, [https://doi.org/10.1175/1520-0493\(2002\)130<2671:TSONSC>2.0.CO;2](https://doi.org/10.1175/1520-0493(2002)130<2671:TSONSC>2.0.CO;2).
- Ashley, W. S., A. M. Haberlie, and J. Strohm, 2019: A climatology of quasi-linear convective systems and their hazards in the United States. *Wea. Forecasting*, **34**, 1605–1631, <https://doi.org/10.1175/WAF-D-19-0014.1>.
- Atkins, N. T., and M. St. Laurent, 2009: Bow echo mesovortices. Part I: Processes that influence their damaging potential. *Mon. Wea. Rev.*, **137**, 1497–1513, <https://doi.org/10.1175/2008MWR2649.1>.
- , J. M. Arnott, R. W. Przybylinski, R. A. Wolf, and B. D. Ketcham, 2004: Vortex structure and evolution within bow echoes. Part I: Single-Doppler and damage analysis of the 29 June 1998 derecho. *Mon. Wea. Rev.*, **132**, 2224–2242, [https://doi.org/10.1175/1520-0493\(2004\)132<2224:VSAEWB>2.0.CO;2](https://doi.org/10.1175/1520-0493(2004)132<2224:VSAEWB>2.0.CO;2).
- Benjamin, T. B., 1968: Gravity currents and related phenomena. *J. Fluid Mech.*, **31**, 209–248, <https://doi.org/10.1017/S0022112068000133>.
- Bryan, G. H., and H. Morrison, 2012: Sensitivity of a simulated squall line to horizontal resolution and parameterization of microphysics. *Mon. Wea. Rev.*, **140**, 202–225, <https://doi.org/10.1175/MWR-D-11-00046.1>.
- , J. C. Wyngaard, and J. M. Fritsch, 2003: Resolution requirements for the simulation of deep moist convection. *Mon. Wea. Rev.*, **131**, 2394–2416, [https://doi.org/10.1175/1520-0493\(2003\)131<2394:RRFTSO>2.0.CO;2](https://doi.org/10.1175/1520-0493(2003)131<2394:RRFTSO>2.0.CO;2).
- Chen, F., and J. Dudhia, 2001: Coupling an advanced land surface-hydrology model with the Penn State–NCAR MM5 modeling system: Part I: Model implementation and sensitivity. *Mon. Wea. Rev.*, **129**, 569–585, [https://doi.org/10.1175/1520-0493\(2001\)129<0569:CAALSH>2.0.CO;2](https://doi.org/10.1175/1520-0493(2001)129<0569:CAALSH>2.0.CO;2).
- Clark, A. J., and Coauthors, 2012: An overview of the 2010 Hazardous Weather Testbed Experimental Forecast Program Spring Experiment. *Bull. Amer. Meteor. Soc.*, **93**, 55–74, <https://doi.org/10.1175/BAMS-D-11-00040.1>.
- Cram, T. A., M. T. Montgomery, and R. F. A. Hertenstein, 2002: Early evolution of vertical vorticity in a numerically simulated idealized convective line. *J. Atmos. Sci.*, **59**, 2113–2127, [https://doi.org/10.1175/1520-0469\(2002\)059<2113:EEOVVI>2.0.CO;2](https://doi.org/10.1175/1520-0469(2002)059<2113:EEOVVI>2.0.CO;2).
- Engerer, N. A., D. J. Stensrud, and M. C. Coniglio, 2008: Surface characteristics of observed cold pools. *Mon. Wea. Rev.*, **136**, 4839–4849, <https://doi.org/10.1175/2008MWR2528.1>.
- Gallo, B. T., A. J. Clark, and S. R. Dembek, 2016: Forecasting tornadoes using convection-permitting ensembles. *Wea. Forecasting*, **31**, 273–295, <https://doi.org/10.1175/WAF-D-15-0134.1>.
- , —, B. T. Smith, R. L. Thompson, I. Jirak, and S. R. Dembek, 2018: Blended probabilistic tornado forecasts: Combining climatological frequencies with NSSL-WRF ensemble forecasts. *Wea. Forecasting*, **33**, 443–460, <https://doi.org/10.1175/WAF-D-17-0132.1>.
- , —, —, —, —, and —, 2019: Incorporating UH occurrence time to ensemble-derived tornado probabilities. *Wea. Forecasting*, **34**, 151–164, <https://doi.org/10.1175/WAF-D-18-0108.1>.
- Hepper, R. M., I. L. Jirak, and J. M. Milne, 2016: Assessing the skill of convection-allowing ensemble forecasts of severe MCS winds from the SSEO. *28th Conf. on Severe Local Storms*, Portland, OR, Amer. Meteor. Soc., 16B.2, <https://ams.confex.com/ams/28SLS/webprogram/Paper300134.html>.
- Iacono, M. J., J. S. Delamere, E. J. Mlawer, M. W. Shephard, S. A. Clough, and W. D. Collins, 2008: Radiative forcing by long-lived greenhouse gases: Calculations with the AER radiative transfer models. *J. Geophys. Res.*, **113**, D13103, <https://doi.org/10.1029/2008JD009944>.
- Janjić, Z. I., 1994: The step-mountain Eta coordinate model: Further developments of the convection, viscous sublayer, and turbulence closure schemes. *Mon. Wea. Rev.*, **122**, 927–945, [https://doi.org/10.1175/1520-0493\(1994\)122<0927:TSMECM>2.0.CO;2](https://doi.org/10.1175/1520-0493(1994)122<0927:TSMECM>2.0.CO;2).
- , 2002: Nonsingular implementation of the Mellor–Yamada Level 2.5 scheme in the NCEP Meso model. NCEP Office Note 437, 61 pp., <https://www.emc.ncep.noaa.gov/officenotes/newernotes/on437.pdf>.
- Johnson, A., X. Wang, F. Kong, and M. Xue, 2013: Object-based evaluation of the impact of horizontal grid spacing on convection-allowing forecasts. *Mon. Wea. Rev.*, **141**, 3413–3425, <https://doi.org/10.1175/MWR-D-13-00027.1>.
- Kain, J. S., and Coauthors, 2008: Some practical considerations regarding horizontal resolution in the first generation of operational convection-allowing NWP. *Wea. Forecasting*, **23**, 931–952, <https://doi.org/10.1175/WAF2007106.1>.
- , S. R. Dembek, S. J. Weiss, J. L. Case, J. J. Levit, and R. A. Sobash, 2010: Extracting unique information from high-resolution forecast models: Monitoring selected fields and phenomena every time step. *Wea. Forecasting*, **25**, 1536–1542, <https://doi.org/10.1175/2010WAF2222430.1>.

- Knupp, K. R., and Coauthors, 2014: Meteorological overview of the devastating 27 April 2011 tornado outbreak. *Bull. Amer. Meteor. Soc.*, **95**, 1041–1062, <https://doi.org/10.1175/BAMS-D-11-00229.1>.
- Loken, E. D., A. J. Clark, M. Xue, and F. Kong, 2017: Comparison of next-day probabilistic severe weather forecasts from coarse- and fine-resolution CAMs and a convection-allowing ensemble. *Wea. Forecasting*, **32**, 1403–1421, <https://doi.org/10.1175/WAF-D-16-0200.1>.
- Mellor, G. L., and T. Yamada, 1982: Development of a turbulence closure model for geophysical fluid problems. *Rev. Geophys.*, **20**, 851–875, <https://doi.org/10.1029/RG020i004p00851>.
- Mlawer, E. J., S. J. Taubman, P. D. Brown, M. J. Iacono, and S. A. Clough, 1997: Radiative transfer for inhomogeneous atmospheres: RRTM, a validated correlated-k model for the longwave. *J. Geophys. Res.*, **102**, 16 663–16 682, <https://doi.org/10.1029/97JD00237>.
- Naylor, J., M. S. Gilmore, R. L. Thompson, R. Edwards, and R. B. Wilhelmson, 2012: Comparison of objective supercell identification techniques using an idealized cloud model. *Mon. Wea. Rev.*, **140**, 2090–2102, <https://doi.org/10.1175/MWR-D-11-00209.1>.
- Pfost, R. L., and A. E. Gerard, 1997: “Bookend vortex” induced tornadoes along the Natchez Trace. *Wea. Forecasting*, **12**, 572–580, [https://doi.org/10.1175/1520-0434\(1997\)012<0572:BVTAT>2.0.CO;2](https://doi.org/10.1175/1520-0434(1997)012<0572:BVTAT>2.0.CO;2).
- Potvin, C. K., and M. L. Flora, 2015: Sensitivity of idealized supercell simulations to horizontal grid spacing: Implications for Warn-on-Forecast. *Mon. Wea. Rev.*, **143**, 2998–3024, <https://doi.org/10.1175/MWR-D-14-00416.1>.
- Powers, J. G., and Coauthors, 2017: The Weather Research and Forecasting Model: Overview, system efforts, and future directions. *Bull. Amer. Meteor. Soc.*, **98**, 1717–1737, <https://doi.org/10.1175/BAMS-D-15-00308.1>.
- Przybylinski, R. W., 1995: The bow echo: Observations, numerical simulations, and severe weather detection methods. *Wea. Forecasting*, **10**, 203–218, [https://doi.org/10.1175/1520-0434\(1995\)010<0203:TBEONS>2.0.CO;2](https://doi.org/10.1175/1520-0434(1995)010<0203:TBEONS>2.0.CO;2).
- , and G. K. Schmocker, 1993: The evolution of a widespread convective windstorm event over central and Eastern Missouri. Preprints, *13th Conf. on Weather Analysis and Forecasting*, Vienna, VA, Amer. Meteor. Soc., 461–465.
- Rotunno, R., J. B. Klemp, and M. L. Weisman, 1988: A theory for strong, long-lived squall lines. *J. Atmos. Sci.*, **45**, 463–485, [https://doi.org/10.1175/1520-0469\(1988\)045<0463:ATFSL>2.0.CO;2](https://doi.org/10.1175/1520-0469(1988)045<0463:ATFSL>2.0.CO;2).
- Schwartz, C. S., and R. A. Sobash, 2019: Revisiting sensitivity to horizontal grid spacing in convection-allowing models over the central and eastern United States. *Mon. Wea. Rev.*, **147**, 4411–4435, <https://doi.org/10.1175/MWR-D-19-0115.1>.
- , and Coauthors, 2009: Next-day convection-allowing WRF Model guidance: A second look at 2-km versus 4-km grid spacing. *Mon. Wea. Rev.*, **137**, 3351–3372, <https://doi.org/10.1175/2009MWR2924.1>.
- , G. S. Romine, K. R. Fossell, R. A. Sobash, and M. L. Weisman, 2017: Toward 1-km ensemble forecasts over large domains. *Mon. Wea. Rev.*, **145**, 2943–2969, <https://doi.org/10.1175/MWR-D-16-0410.1>.
- Skamarock, W. C., and Coauthors, 2008: A description of the Advanced Research WRF version 3. NCAR Tech. Note NCAR/TN-475+STR, 113 pp., <https://doi.org/10.5065/D68S4MVH>.
- Smith, B. T., R. L. Thompson, J. S. Grams, C. Broyles, and H. E. Brooks, 2012: Convective modes for significant severe thunderstorms in the contiguous United States. Part I: Storm classification and climatology. *Wea. Forecasting*, **27**, 1114–1135, <https://doi.org/10.1175/WAF-D-11-00115.1>.
- Sobash, R. A., J. S. Kain, D. R. Bright, A. R. Dean, M. C. Coniglio, and S. J. Weiss, 2011: Probabilistic forecast guidance for severe thunderstorms based on the identification of extreme phenomena in convection-allowing model forecasts. *Wea. Forecasting*, **26**, 714–728, <https://doi.org/10.1175/WAF-D-10-05046.1>.
- , G. S. Romine, C. S. Schwartz, D. J. Gagne II, and M. L. Weisman, 2016: Explicit forecasts of low-level rotation from convection-allowing models for next-day tornado prediction. *Wea. Forecasting*, **31**, 1591–1614, <https://doi.org/10.1175/WAF-D-16-0073.1>.
- , C. S. Schwartz, G. S. Romine, and M. L. Weisman, 2019: Next-day prediction of tornadoes using convection-allowing models with 1-km horizontal grid spacing. *Wea. Forecasting*, **34**, 1117–1135, <https://doi.org/10.1175/WAF-D-19-0044.1>.
- Squitiere, B. J., and W. A. Gallus Jr., 2020: On the forecast sensitivity of MCS cold pools and related features to horizontal grid-spacing in convection-allowing WRF simulations. *Wea. Forecasting*, **35**, 325–346, <https://doi.org/10.1175/WAF-D-19-0016.1>.
- Tegen, I., P. Hollrig, M. Chin, I. Fung, D. Jacob, and J. Penner, 1997: Contribution of different aerosol species to the global aerosol extinction optical thickness: Estimates from model results. *J. Geophys. Res.*, **102**, 23 895–23 915, <https://doi.org/10.1029/97JD01864>.
- Thielen, J. E., and W. A. Gallus Jr., 2019: Influences of horizontal grid spacing and microphysics on WRF forecasts of convective morphology evolution for nocturnal MCSs in weakly forced environments. *Wea. Forecasting*, **34**, 1495–1517, <https://doi.org/10.1175/WAF-D-18-0210.1>.
- Thompson, G., P. R. Field, R. M. Rasmussen, and W. D. Hall, 2008: Explicit forecasts of winter precipitation using an improved bulk microphysics scheme. Part II: Implementation of a new snow parameterization. *Mon. Wea. Rev.*, **136**, 5095–5115, <https://doi.org/10.1175/2008MWR2387.1>.
- Thompson, R. L., B. T. Smith, J. S. Grams, A. R. Dean, and C. Broyles, 2012: Convective modes for significant severe thunderstorms in the contiguous United States. Part II: Supercell and QLCS tornado environments. *Wea. Forecasting*, **27**, 1136–1154, <https://doi.org/10.1175/WAF-D-11-00116.1>.
- Trapp, R. T., and M. L. Weisman, 2003: Low-level mesovortices within squall lines and bow echoes. Part II: Their genesis and implications. *Mon. Wea. Rev.*, **131**, 2804–2823, [https://doi.org/10.1175/1520-0493\(2003\)131<2804:LMWSLA>2.0.CO;2](https://doi.org/10.1175/1520-0493(2003)131<2804:LMWSLA>2.0.CO;2).
- Trapp, R. J., S. A. Tessendorf, E. S. Godfrey, and H. E. Brooks, 2005: Tornadoes from squall lines and bow echoes. Part I: Climatological distribution. *Wea. Forecasting*, **20**, 23–34, <https://doi.org/10.1175/WAF-835.1>.
- Trier, S. B., C. A. Davis, D. A. Ahijevych, M. L. Weisman, and G. H. Bryan, 2006: Mechanisms supporting long-lived episodes of propagating nocturnal convection within a 7-day WRF Model simulation. *J. Atmos. Sci.*, **63**, 2437–2461, <https://doi.org/10.1175/JAS3768.1>.
- VandenBerg, M. A., M. C. Coniglio, and A. J. Clark, 2014: Comparison of next-day convection-allowing forecasts of storm motion on 1- and 4-km grids. *Wea. Forecasting*, **29**, 878–893, <https://doi.org/10.1175/WAF-D-14-00011.1>.
- Wakimoto, R. H., H. V. Murphy, C. A. Davis, and N. T. Atkins, 2006: High winds generated by bow echoes. Part II: The relationship between the mesovortices and damaging straight-line

- winds. *Mon. Wea. Rev.*, **134**, 2813–2829, <https://doi.org/10.1175/MWR3216.1>.
- Weisman, M. L., 1993: The genesis of severe long-lived bow echoes. *J. Atmos. Sci.*, **50**, 645–670, [https://doi.org/10.1175/1520-0469\(1993\)050<0645:TGOSLL>2.0.CO;2](https://doi.org/10.1175/1520-0469(1993)050<0645:TGOSLL>2.0.CO;2).
- , and C. A. Davis, 1998: Mechanisms for the generation of mesoscale vortices within quasi-linear convective systems. *J. Atmos. Sci.*, **55**, 2603–2622, [https://doi.org/10.1175/1520-0469\(1998\)055<2603:MFTGOM>2.0.CO;2](https://doi.org/10.1175/1520-0469(1998)055<2603:MFTGOM>2.0.CO;2).
- , and R. T. Trapp, 2003: Low-level mesovortices within squall lines and bow echoes. Part I: Overview and dependence on environmental shear. *Mon. Wea. Rev.*, **131**, 2779–2803, [https://doi.org/10.1175/1520-0493\(2003\)131<2779:LMWSLA>2.0.CO;2](https://doi.org/10.1175/1520-0493(2003)131<2779:LMWSLA>2.0.CO;2).
- , and R. Rotunno, 2004: A theory for strong long-lived squall lines. *J. Atmos. Sci.*, **61**, 361–382, [https://doi.org/10.1175/1520-0469\(2004\)061<0361:ATFSL>2.0.CO;2](https://doi.org/10.1175/1520-0469(2004)061<0361:ATFSL>2.0.CO;2).
- , C. Davis, W. Wang, K. W. Manning, and J. B. Klemp, 2008: Experiences with 0–36-h explicit convective forecasts with the WRF-ARW Model. *Wea. Forecasting*, **23**, 407–437, <https://doi.org/10.1175/2007WAF2007005.1>.
- , C. Evans, and L. Bosart, 2013: The 8 May 2009 superderecho: Analysis of a real-time explicit convective forecast. *Wea. Forecasting*, **28**, 863–892, <https://doi.org/10.1175/WAF-D-12-00023.1>.
- , and Coauthors, 2015: The Mesoscale Predictability Experiment (MPEx). *Bull. Amer. Meteor. Soc.*, **96**, 2127–2149, <https://doi.org/10.1175/BAMS-D-13-00281.1>.
- Wheatley, D. M., and R. J. Trapp, 2008: The effect of mesoscale heterogeneity on the genesis and structure of mesovortices within quasi-linear convective systems. *Mon. Wea. Rev.*, **136**, 4220–4241, <https://doi.org/10.1175/2008MWR2294.1>.
- Xu, X., M. Xue, and Y. Wang, 2015: Mesovortices within the 8 May 2009 bow echo over the central United States: Analyses of the characteristics and evolution based on Doppler radar observations and a high-resolution model simulation. *Mon. Wea. Rev.*, **143**, 2266–2290, <https://doi.org/10.1175/MWR-D-14-00234.1>.